DEPARTMENT OF CHEMISTRY, UNIVERSITY OF JYVÄSKYLÄ RESEARCH REPORT No. 205

NON-LINEAR INTERACTIONS OF FEMTOSECOND LASER PULSES WITH GRAPHENE: PHOTO-OXIDATION, IMAGING AND PHOTODYNAMICS

BY

JUHA KOIVISTOINEN

Academic Dissertation for the Degree of
Doctor of Philosophy

To be presented, by permission of the Faculty of Mathematics and Science of the University of Jyväskylä, for public examination in Auditorium KEM1, on November 10th, 2017 at 12 noon.

UNIVERSITY OF JYVÄSKYLÄ

ISBN 978-951-39-7214-1
ISBN 978-951-39-7215-8 (PDF)
ISSN 0357-346X

ABSTRACT

Koivistoinen, Juha
Non-linear interactions of femtosecond laser pulses with graphene: photo-oxidation, imaging and photodynamics.
Jyväskylä: University of Jyväskylä, 2017, 68 p.
Department of Chemistry. University of Jyväskylä. Report 205
ISSN-0357-346X
978-951-39-7214-1 (nidottu)
978-951-39-7215-8 (PDF)

This thesis presents a study focused on interactions of femtosecond laser pulses with graphene, a one atom thick carbon membrane.
Graphene, which exhibits exceptional electronic and optoelectronic properties, could provide considerable advantage over current silicon-based electronics. Graphene alone, being semi-metal, is not sufficient for electronic applications, but requires modification. For this, a set of methods for modifying and measuring the properties of graphene was developed.
With the perspective of making graphene a suitable component for electronics, optoelectronics or photonics, ultrashort laser pulses were used for drawing patterns on graphene. The procedure modifies graphene chemically by photo-oxidation, and physically, by opening a gap to its electronic band structure, changing graphene into a semiconductor. During the process, the band gap can be increased to the extent, where the material becomes an insulator.
It was observed in topographic studies that photo-oxidation begins at point-like sources and expands into islands of oxidized graphene, which eventually merge together. This is because the probability that new oxidation occurs in close proximity to an already oxidized area is five orders of magnitude greater than the probability of oxidation elsewhere on graphene. Also, accompanying the oxidation process, a third-order nonlinear signal arising from the graphene, diminishes, providing a contrast mechanism for optical imaging. Additionally, the Raman spectrum shows notable changes in the position of the G-band and increase in intensity of the D-band.
Further insight into the patterned structures was obtained with micro--X-ray photoelectron spectroscopy. The initial steps of patterning only change the ratio of sp^2/sp^3 carbons in the material but the degree of oxidation increases after the islands coalesce. With higher irradiation doses the proportion of hydroxyl and epoxide groups increases, finally reaching the level of ~65 %.
The Four-wave mixing (FWM) signal of graphene was monitored during the oxidation process. By utilizing the extraordinarily strong non-linear optical response of graphene FWM spectroscopy was combined with wide-field microscopy, allowing the patterning process to be followed in real-time. Femtosecond wide-field FWM microscopy was proven as fast large area imaging technique for characterization of graphene and observing changes in graphene in real-time.

Time-resolved coherent anti-Stokes Raman scattering measurement (CARS) was applied to graphene and a G-mode dephasing time was recorded. Additionally, it was shown that by utilizing BOXCARS excitation geometry various nonlinear optical processes could be unambiguously separated and measured simultaneously. The short dephasing time ($T_2/2$) of the G-mode (325 fs) was explained with dynamically changing G-mode frequency and width accompanied with relaxation of excited charge carrier population, due to non-adiabatic coupling between phonons and electrons in graphene.

Keywords: Nonlinear intearctions, graphene, CARS, Raman, photo-oxidation

Author
Juha Koivistoinen
Department of Chemistry
Nanoscience Center
University of Jyväskylä
P.O. Box 35
FI-40014 University of Jyväskylä
Finland
juha.t.koivistoinen@jyu.fi

Supervisors
Professor Mika Pettersson
Department of Chemistry
Nanoscience Center
University of Jyväskylä
P.O. Box 35
FI-40014 University of Jyväskylä
Finland

Reviewers
Professor Thomas Huser
Faculty of Physics
University of Bielefeld
Germany

Professor Achim Hartschuh
Department of Chemistry and Center for nanoscience
Ludwig-Maximilian University of Munich
Germany

Opponent
Professor Eric Potma
Department of Chemistry
University of California, Irvine
USA

PREFACE

The work presented in this thesis was performed at the University of Jyväskylä between 2014 and 2017. My past years as a doctoral student been filled with enthusiasm and joy, but also occational frustration. Although, these years have been demanding, but it has also taught me so much. Nothing drives us forward mor than new challenges, accompanied with environment full of capable, experienced and intelligent people. This is what doctoral school provides and what also makes it irriplaceable. It is educational in so many levels.

I have had an honor to have such a great people for my help and support during the project. For this, I want to express my deepest graditude to my principal instructor Professor Mika Pettersson for the interesting project and all the support and guidance. You are a visionary as a scientist and an awesome boss. Dr. Pasi Myllyperkiö, thank you for your assistance with all technical aspects in the lab. This combined with your effort in building all the measurement setups made it possible for me to finnish my project.

I want to thank my reviewers Professors Achim Hartschuh and Thomas Huser for making time to review my thesis. The financial support from University of Jyväskylä, including travel expenses, which enabled me to participate on international conferences, meet the fellow scientists and learn about their interesting projects, is greatly acknowledged.

I also want to thank my co-workers and group members at the NCS and Department of Chemistry, for making the work more pleasurable. It's been a pleasure to work with you all. I miss the coffee room talks and atmosphere at the NSC and it would still be fun to participate the side activities such as Solvent Section (Liuotin jaosto) meetings and Christmas party band sessions.

Finally, I want to thank the people closest to me. My friends for keeping me real and offering me a break from science every now and then, thank you for that. My family: thank you for offering me all the support over these years, and beliving in me in every step of my life. Annika: Thank you for putting up with me. I know I can be difficult to live with, especially in stressful times, but I hope you stand by me in the future as you have so far. I want you to know that your love and support means a world to me.

Early October Jyväskylä 2017
Juha Koivistoinen

LIST OF PUBLICATIONS

The publications, contributed by the author, that are included in this thesis:

I. J. Aumanen, A. Johansson, **J. Koivistoinen**, P. Myllyperkiö, M. Pettersson. Patterning and tuning of electrical and optical properties of graphene by laser induced two-photon oxidation. *Nanoscale*, **2015**, 7, 2851.

II. **J. Koivistoinen**, L. Sladkova, J. Aumanen, P. Koskinen, K. Roberts, A. Johansson, P. Myllyperkiö, M. Pettersson. From seeds to islands: Growth of oxidized graphene by two-photon oxidation. *J. Phys. Chem. C*, **2016**, 120 (39), 22330–22341

III. A. Johansson, H-C. Tsai, J. Aumanen, **J. Koivistoinen**, P. Myllyperkiö, Y-Z. Hung, M-C. Chuang, C-H. Chen, W. Y. Woon, M. Pettersson. Chemical composition of two photon-oxidized graphene. *Carbon* **2017**, 115, 77-82.

IV. **J. Koivistoinen**, J. Aumanen, V-M. Hiltunen, P. Myllyperkiö, A. Johansson, M. Pettersson. Real-time monitoring of graphene patterning with wide-field four-wave mixing microscopy. *Applied Physics Letters*, **2016**, 108, 153112.

V. **J. Koivistoinen**, P. Myllyperkiö, M. Pettersson. Time-Resolved coherent anti-Stokes Raman scattering of graphene: Dephasing Dynamics of Optical Phonon. *J. Phys. Chem. Lett.*, **2017**, 8, 4108–4112. (Correction submitted)

For publications II, IV and V the author is the first author, and has performed Raman measurements and all the analysis of Raman data. In IV and V the author has carried out wide-field FWM and CARS measurements and contributed to the building of the wide-field FWM setup. The author has written the initial versions of papers IV and V. For papers I and III, the author has contributed by executing the Raman measurements and involved in writing the paper.

List of publications the author has contributed which are **not** included in this thesis:

a. C. Caputo, **J. Koivistoinen,** J. Moilanen, J. Boynton, H. Tuononen, P. P. Power. Counterintuitive mechanisms of the addition of hydrogen and simple olefins to heavy group 13 alkene analogues. *Journal of the American Chemical Society*, **2013**, 135(5), 1952-60.

b. L. Koskinen, P. Hirva, A. Hasu, S. Jääskelainen, **J. Koivistoinen**, M. Pettersson, M. Haukka. Modification of the supramolecular structure of [(thione)IY] (Y = Cl, Br) systems by cooperation of strong halogen bonds and hydrogen bonds. *CrystEngComm* **2015**, 17(13), 2718-2727.

c. M. J. Hokkanen, S. Lautala, D. Shao, T. Turpeinen, **J. Koivistoinen**, M. Ahlskog. On-chip purification via liquid immersion of arc-discharge synthesized multiwalled carbon nanotubes. *Applied Physics A: Materials Science & Processing,* **2016**, 122(7), 1-8.

d. I. Kondrasenko, K-y. Chung, Y-T. Chen, **J. Koivistoinen**, E. V. Grachova, A. Karttunen, P-T. Chou, I. O. Koshevoy. Harnessing Fluorescence versus Phosphorescence Ratio via Ancillary Ligand Fine-Tuned MLCT Contribution. *Journal of Physical Chemistry C,* **2016**, 120(22), 12196-12206.

CONTENTS

1 INTRODUCTION

The majority of the living population have stared at graphene for years, unaware of its existence. This is because the tip of a pencil mostly consists of carbon as in its most stable form - graphite - which in turn is composed of numrous graphene sheets.

Graphene is a one-atom thick carbon membrane, where the carbon atoms are bound to one another forming a network of planar hexagonal shapes.[1, 2] This binding, governed by electronic properties of the carbon atom, has resulted in a rather peculiar material. The electronic structure of graphene, with electrons behaving like massless particles and zero bandgap, leads to high electron mobility, thermal conductivity, mechanical stability, non-linear optical response, etc.[3-8]

Because of its astonishing properties, graphene is considered a viable candidate for applications in numerous fields and particularly for printed electronics, sensors, photodetectors, touch screens, photovoltaic cells, high frequency transistors, quantum dot displays and transparent electronics.[9-15] Since graphene is a semi-metal, these applications are mostly designed as graphene incorporated devices, where graphene is used as a component of a larger device. With the intention of building graphene-based devices, properties of graphene alone are not enough to meet the demands of the proposed applications; semiconducting and insulating components are needed too.

By taking advantage of nonlinear light matter interactions of graphene, selected parts of graphene can be controllably modified into graphene oxide, which is a semiconductor.[16] Thus, during the modification, the bandgap of graphene is opened and can be further increased until the material becomes insulating. The oxidative patterning is a single-step method, which is performed in ambient air and provides all components needed to build electronic devices, such as transistors (Paper I).

In this Thesis, nonlinear optical interactions were used for modifying graphene and for writing patterns on it, for imaging the patterns, and for investigating photodynamical processes in graphene. The oxidation patterning was imaged in real time, utilizing a method where the strong FWM signal acquired from

graphene and wide-field microscopy are combined, resulting in femtosecond FWM wide-field microscopy. Time-resolved coherent anti-Stokes Raman scattering (TR-CARS) was applied to gain knowledge on time-dependent behavior of Raman active modes in graphene. Interestingly, CARS measurement also provides indirect information on the relaxation of the hot electron gas.
In future, the wide-field imaging and time-resolved CARS can be combined in order to visualize the signal evolution in space and time after pulsed excitation.

1.1 Graphene

In 2004, a groundbreaking study of graphene, single crystal, one-atom thick carbon material, was published.[17] This discovery led to a Nobel Prize in Physics, in 2010, for Andre Geim and Konstantin Novoselov. Their discovery started a graphene gold-rush era, resulting in an explosion of graphene-related published papers and patents. The peak of the rush has already passed but still, thousands of studies related to graphene are published annually. During the writing of the present thesis, a Web of Science search of "graphene" yielded over 80,000 papers published in the past five years alone. Due to its unusual physical properties, graphene has also caught the eye of various industries, which have invested billions of dollars in its R&D.[18]

1.1.1 Chemical Structure

In nature, carbon exists in various allotropes, different microscopic forms under the same physical conditions, such as diamond and graphite. Of all the existing allotropes, the most stable form (i.e. standard state) of carbon, is graphite. Graphite is composed of numerous sheets of graphene, which are held together by dispersion forces. Each one of these graphene sheets is ~335 ± 10 pm (1 pm = 10^{-12} m) thick.[19]

Atomic structure of material is predetermined by its electronic structure. Electronic configuration of carbon ($1s^2 2s^2 2p^2$) governs the bonding of carbon to its neighboring atoms and allows carbon to form single, double and triple covalent bonds, combining the bonding 2s- and 2p-orbitals into sp^3, sp^2, and sp-hybrid orbitals, respectively.[20] Valence bond (VB) theory states that a carbon atom which forms only single covalent bonds to its neighbors exhibits electronic configuration $1s^2 2(sp^3)^4$. Double covalent bonded carbon possesses $1s^2 2(sp^2)^3 2p^1$ electronic configuration, whereas the triple bonded carbon has electron configuration $1s^2 2(sp)^2 2p^2$.[20] The hybridization with respect to the carbon results in tetrahedral (e.g., in diamonds), planar (e.g., in graphene, carbon nanotubes), or linear (e.g., acetylene, carbon monoxide) structure with carbon hybridizations sp^3, sp^2, and sp, respectively. The carbon-carbon single bond (C-C) is formed as a combination of two sp^3 hybrid orbitals and is stated as a σ bond, whereas the carbon-carbon double bond (C=C) forms a σ bond as a combination of two sp^2 orbitals, leaving the p orbital to form a π bond with the bonded counterpart. For

triple bond, the sp orbitals form a σ bond and two π bonds are created as a combination of the remaining p orbitals and their matching part in the neighboring atom. In terms of molecular orbital (MO) theory, as two carbon atoms are bonded, bonding 1σ and antibonding $1\sigma^*$ orbitals are formed by combining 2s-orbitals from adjacent carbons. Also, p_z-orbitals in both carbons form bonding 2σ and antibonding $2\sigma^*$ orbitals. The remaining two 2p-orbitals (p_x and p_y) in both atoms form in total four π-orbitals, two bonding π and two antibonding π^* orbitals. Of the eight formed molecular orbitals 1σ, $1\sigma^*$, and two π orbitals are fully occupied, resulting in bond order two.

VB theory describes materials with multiple adjacent sp^2-carbons as a resonance structure where the double bonding is delocalized over the entire sp^2-region. MO theory predicts the valence electrons of sp^2-bonded carbons to reside in the π-orbitals. The preferred bond order in carbon-carbon bond points toward sp^2-hybridization and trigonal planar structure. If such structure is extended to larger network of cyclic carbon compounds, such as benzene, naphthalene or coronene; the result is a planar structure with π-electrons delocalized over the entire compound. Growing the planar carbon net further the material eventually becomes graphene. In principle, graphene can be thought of as a two-dimensional polymer, a periodic hexagonal carbon net composed of two-carbon subunits with electron density delocalized over the entire compound (FIGURE 1). Such delocalization result in shortening of the carbon-carbon

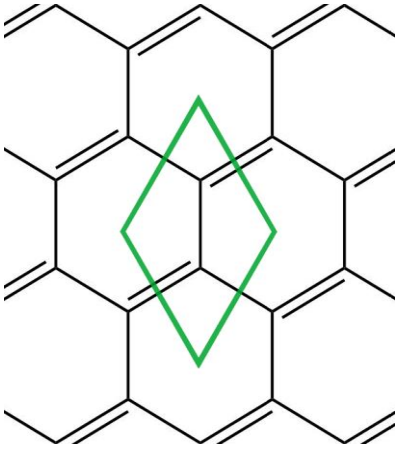

FIGURE 1 Representation of molecular structure of graphene. The entire graphene sheet can be constructed from two atom subunit (green frame).

bonds.

As governed by the Pauli Exclusion Principle, two electrons in the system cannot occupy the exact same quantum state. For atoms and molecules, the energies of electronic states are discrete. As the number of atoms in a system increases, the number of electronic states increases as well. This results in an energy difference between occupied (and unoccupied) states, which decreases with increasing size of the system. In solids, the number of atoms in the system is so vast that the energy spacing between two distinct occupied (or unoccupied) states is practically indistinguishable and the states are depicted as a continuum

of states. As the discrete energies of specific states are not known, the number of states in an infinitesimal energy region is evaluated and stated as density of states (DOS). Generally, as molecules exhibit an energy gap between their highest occupied molecular orbital (HOMO) and lowest unoccupied molecular orbital (LUMO) states, the band structure of solids may also exhibit a band gap between valence (occupied) band and conduction (unoccupied) band as states with only certain energies are allowed by quantum mechanics. However, for cyclic conjugated carbon compounds the band gap decreases as the number of atoms in the system increases, ultimately forming a periodic two-dimensional lattice. In FIGURE 2, aromatic hydrocarbons, increasing in size toward graphene, possess orbitals an exactly half-filled by electrons. Also, graphene exhibits exactly half-filled band structure. This non-existent band gap gives rise to a vast variety of extraordinary properties.[21]

The band structure also deviates from a molecular point-of-view in its depiction: it is portrayed in momentum space. To describe the entire periodic lattice, a smallest non-divisible unit, Brillouin Zone, is defined in the reciprocal space and the lattice is expanded. For graphene the Brillouin Zone (FIGURE 3a) is a set of two three atom sub sets, and the edges of these subsets are labeled K and K′ points, respectively. The energies of valence band and conduction band, in graphene join at K and K′ (Dirac Point), where the density of states is also zero and Fermi energy of undoped graphene resides (FIGURE 3b).

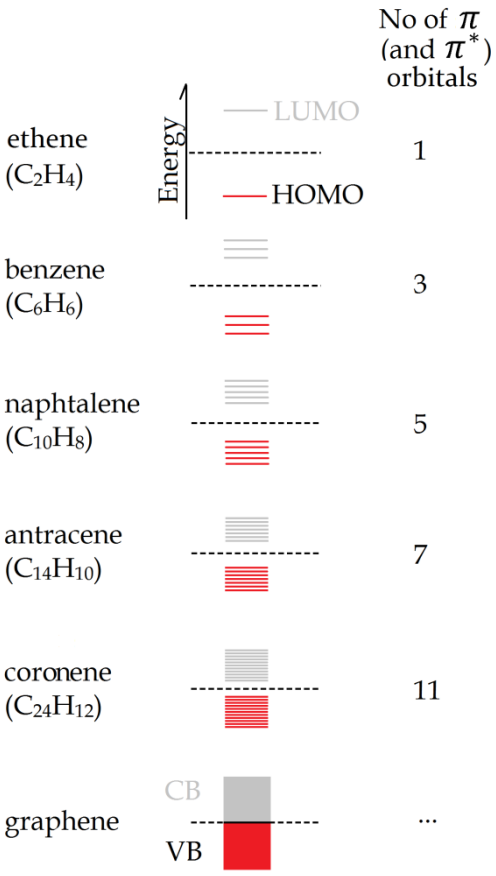

FIGURE 2. A schematic description of band structure of graphene resulting from increasing amount of carbon atoms in the system. The energy difference between occupied (red) (and unoccupied (gray)) states diminishes as does the HOMO-LUMO gap, until they merge at fermi level (dashed line). The system remains half-filled.

Experiments have shown that relativistic quantum mechanics is needed to correctly describe the energy spectrum of graphene because the energy of band structure of graphene near Dirac point (FIGURE 3; $\boldsymbol{k} = \boldsymbol{K}$ (or $\boldsymbol{K}'$)), follows linear dispersion relation.[21-23]

$$E = \hbar v_F |\boldsymbol{k}| \tag{1}$$

where E is the electronic energy, $\hbar$ is Planck's constant divided by 2π and $\boldsymbol{k}$ is the wave–vector associated to crystal momentum $\boldsymbol{p}_{\boldsymbol{crystal}} = \hbar\boldsymbol{k}$, which is measured relative to $\boldsymbol{K}$ or $\boldsymbol{K}'$ points. v_F is Fermi velocity, which is the velocity of electrons consistent with a kinetic energy equal to Fermi energy. This behavior is strictly identical to that of the spectrum of 2D massless electron gas.[21]

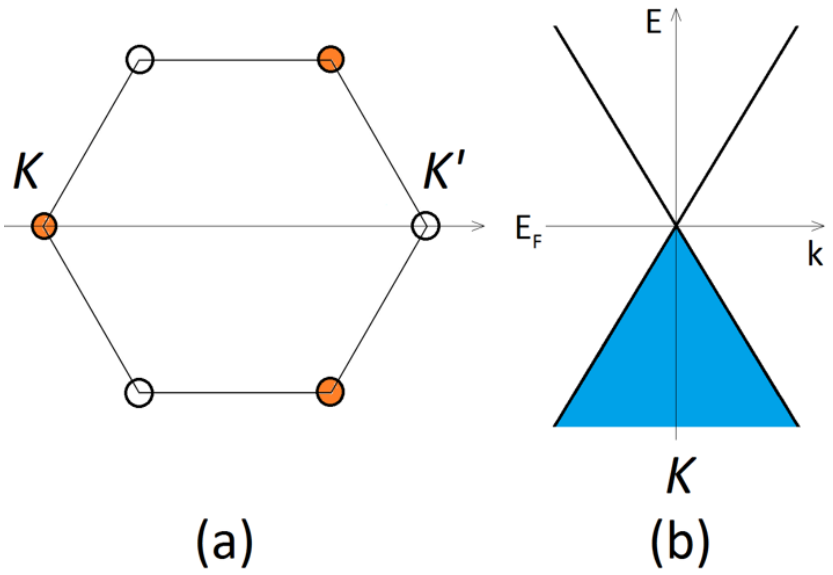

FIGURE 3 (a) Energy diagram of band structure of graphene. The vertical and horizontal axes represent energy and momentum. The cone opening up is the conduction band and the cone opening down is the valence band. E_F is the Fermi energy which is defined by the energy level of the carriers (blue color). The white color above E_F depicts holes. There is no energy gap between valence and conduction band. (b) Brillouin zone of graphene where the ***K*** and ***K'*** are depicted.

1.1.2 Properties and applications

The electronic structure of graphene results in a very high carrier mobility. For suspended, annealed high quality graphene 185,000 $cm^2V^{-1}s^{-1}$ has been reported.[24] Even with a limitation to mobility, placed by impurities, substrate and optical phonon vibrations etc., at room temperature a mobility as high as 20,000 $cm^2V^{-1}s^{-1}$ can be achieved.[25, 26] Linear optical absorbance of graphene, in visible spectral range, is 2.3% and depends solely on natural constants.[27] In terahertz region, the absorbance increases with energy.[28] In addition, suspended graphene outperforms carbon nanotubes (CNT) in thermal conductivity, with value of 5300 W/mK.[6] When graphene is on a substrate the heat conduction changes slightly but still the in-plane thermal conductivity is two orders of magnitude larger than between graphene and the substrate.[29, 30] Due to the zero bandgap and linear dispersion relation the Fermi level can be adjusted by applying an electrostatic field.[31] Graphene also exhibits more exotic phenomena such as breakdown of adiabatic Born-Oppenheimer approximation, quantum Hall effect and Klein paradox.[31-34]

1.1.2.1 Applicability

Graphene is transparent and conducts electricity and heat better than any metal, so it is an ideal candidate to replace current indium tin oxide (ITO)-based materials.[35] Indium is scarcer and more expensive than carbon and a challenging material with which to build flexible devices.[36] High-speed graphene circuits with high-bandwidths have been demonstrated already.[9] Applicability of graphene in printed electronics has been demonstrated on several substrates with graphene inks.[37, 38] The potential of graphene as a material for flexible elec-

tronics applications as a combination of high frequency electronics is possibly useful in the "IoT" era.[39, 40] The other demonstrated or predicted electronics-related applications that graphene and related materials could either replace or improve upon include memory cells and logic gates which are used in multiple fields of modern integrated electronics.[35, 41-43] Graphene is a conductor with a zero band gap. Because semiconductors and insulators are also required for electronics applications, an approach to open the band gap in graphene is needed. Hydrogenation and fluorination of graphene has been shown to give rise to semiconducting and insulating graphene related materials.[44, 45]

Fabricating functional graphene prototypes of touch screens, rollable E-papers and organic light emitting diodes (OLED) are expected before 2020, which is sooner than RF or logic transistors.[18] That is mainly because the production of graphene with sufficient quality at industrial scale is still under development and the three examples just mentioned could be functional with medium quality graphene related materials.

Optoelectronic devices, especially photodetectors, ultrafast lasers, and THz wave detectors are in a point of interest of graphene applications.[46-48] Because of the two-dimensional structure and high chemical potential of graphene, its conductance is sensitive to perturbation, and thus suitable for photogating.[49] Conversion of photons in the IR and THz regions to graphene plasmons has been demonstrated, and can further enhance photodetection in these regions.[50, 51] Additionally, THz detection opens up new applications such as bolometers, cameras and broadband antennas, while THz operation opens up a possibility for high data transmission rates for wireless data transfer applications.[51-55] Also, lasers where graphene functions as a saturable absorber, have been designed, with wide tunability and bandwidth, thus being a useful asset for telecommunications applications.[56]

Graphene and related materials can also prove useful sensors for larger particles or as chemical or biological sensors.[57, 58] Indeed, potential of graphene and related materials for gas sensing has been demonstrated.[59] Because graphene is flexible, transparent, and sustains a significant amount of mechanical stress, it is ideal for strain sensors when integrated with polymers, which has been demonstrated with epoxy gloves.[60]

Graphene could lead to completely new approaches, such as spintronics, where the spin state of the electron is utilized in addition to electric current.[61, 62] Possible applications are quantum computing and memory units and new types of memory.[63, 64] Additionally, graphene is anticipated to give rise to or to improve numerous applications in biomedicine, and energy storage and conversion.[65-67] Overall, the major impact of graphene and related carbon-based two-dimensional materials on applications is expected to take place by integrating graphene-based devices with existing technology. This development is expected to take place in the coming years, whereas stand-alone graphene-based devices will be seen later in future.

1.1.3 Synthesis

The most common procedure for graphene synthesis is the chemical vapor deposition (CVD), where a metal foil, usually Cu or Ni, is placed in a heating chamber which is then filled with a carbon-containing gas, such as methane (CH_4), methanol (CH_3OH) or ethanol (CH_3CH_2OH), at elevated temperatures (T < 1100 ^{O}C).[68-70] In the process, graphene is formed on the metal foil, whence it is transferred to another substrate. Although other metals have been tried as replacements for copper and nickel, CVD procedure with copper has been found to produce the largest area coverage and only few defects and areas with double layer. [70-72] Transfer is an additional step in the production, and a more ideal approach would be to grow graphene directly on the final substrate.[73]

Other synthesis methods, such as mechanical exfoliation, epitaxial growth on SiC, unzipping CNTs, and plasma enhanced CVD (PECVD) have proven to be less applicable in practice than CVD with Cu catalyst, when product quality, or quantity or production time and complexity are considered, overall.[74-77] Hence, CVD is a method, for which the flaws and advantages of graphene synthesis are considered well balanced and which enables synthesis of large amounts of graphene of sufficient quality. All the graphene samples utilized in the experiments presented in this thesis are synthesized by CVD method.

1.1.4 Graphene oxide

Analogous to graphene, graphene oxide (GO) is a single sheet of graphite oxide. Unlike graphene, GO is a semiconducting hydrophilic material, which also produces fluorescence. The fluorescence has been suggested to originate, not from the oxygen containing chemical groups, but from sp^2 carbon areas confined by the oxygen containing groups.[78]

The definitive structure of GO has been under a debate in terms of nature and diffusion of oxygen containing chemical groups.[79] GO is loosely defined as graphene, with oxygen to carbon content (at. %) of 20 - 45.[80] The sheet contains oxygen containing functional groups, such as hydroxyl (–OH), carbonyl (C=O), epoxide (C-O-C) and carboxylic acid (-COOH) groups.[80] The distribution of the different oxygen containing groups in GO is thought to be amorphous, and is dependent on the production method. The schematic structure of GO is presented in FIGURE 4.

Graphite oxide has been produced chemically from graphite since the mid nineteenth century and the chemical production technique of graphite oxide is similar today to what it was then, as it involves utilization of acid and an oxidizing agent.[81,82] A recent nuclear magnetic resonance (NMR) study suggests that in chemically produced graphite oxide the oxygen groups are mainly hydroxyl and epoxide groups but some carboxylic acid groups are also present.[83] More precisely, the epoxide group is the proportionally dominating oxygen-containing group in chemically produced GO.[84]

The downsides of chemical synthesis of graphene oxide are wide distribution of structures, the requirement of additional chemicals and long reaction

time. An attempt to locally change the structure of graphene has been demonstrated with UV/ozone treatment, which has shown promising results as nonchemical oxidation method with the ability to control the oxidation.[85]

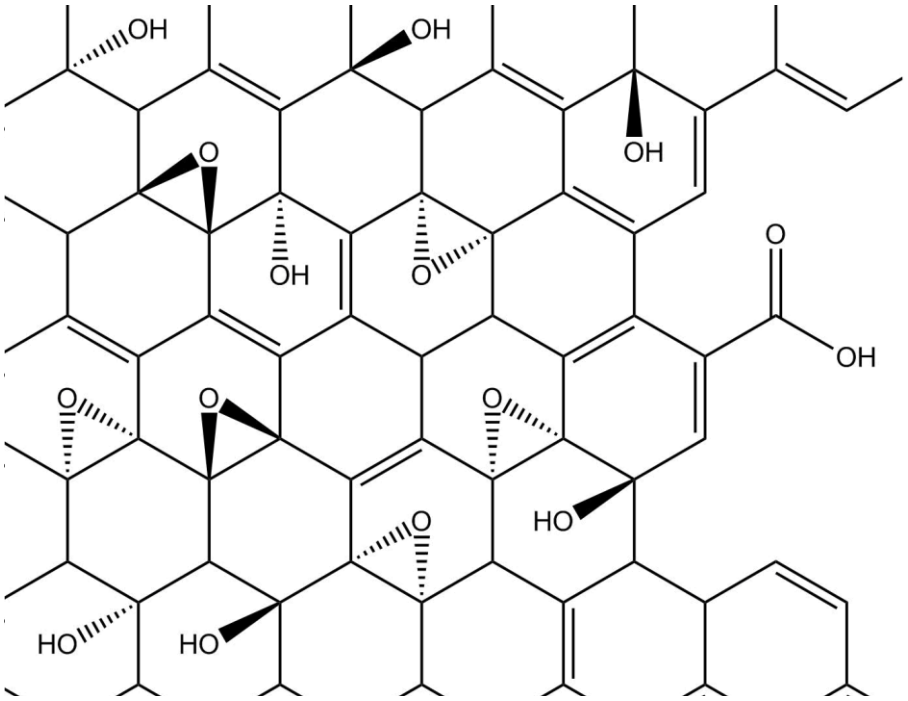

FIGURE 4. Principal chemical structure of GO. The sp^3-type covalent bonding occurs in the middle of the lattice between carbon and hydroxyl and epoxide groups, whereas the carboxylic groups may be present on the edges.

The morphology of GO on surfaces depends on the substrate and the oxidation method. Thermal oxidation results in holes and pits when the oxidation is performed on graphene on SiO_2.[86] However, if thermal oxidation is performed on graphene on hexagonal-boron nitride (h-BN), the degree of oxidation remains minute. Thus, the charge distribution of the substrate has a role in the oxidation process. Photo induced oxidation with UV increases graphene surface roughness but also results in gradual degradation.[85]

Reduced graphene oxide (rGO) is obtained after reduction of graphene oxide as an attempt to make graphene.[87] However, the oxygen content of rGO is still 5%-10%, whereas for graphene it is less than 5%, which could arise from impurities or adsorbed oxygen.[80, 87] Successful reduction of graphite oxide into graphene is also dependent on the type of defects that have been inflicted upon the graphene in the oxidation process.

1.2 Raman spectroscopy

1.2.1 Introduction

The scattering of light from particles much smaller than the wavelength of the incident wave is Rayleigh scattering. Rayleigh scattering is an elastic scattering process, meaning the energy of the scattered photons is the same as for the photons of the excitation source.

Raman scattering is an inelastic scattering process, in which the initial photon loses or gains some of the energy and momentum of the sample.[88] Raman spectroscopy is mainly utilized for characterizing molecular rotations and vibrations but it is also applicable for investigating phonons in solids. (FIGURE 5). For the scattered photon, the energy and momentum are different from those of the exciting photons.

Raman spectrum of a compound (like any vibrational spectrum) is, in principle unique. Raman is considered non-destructive, it requires very little sample preparation and it may be applied to samples in all states of matter. In addition, water does not scatter excessively, making water-soluble materials, such as pharmaceuticals and biomolecules accessible. This is different from IR spectroscopy, where water is heavily absorbing and overlaps, as, for example, with hydroxyl-group (-OH) absorption. In our studies, Raman is used in order

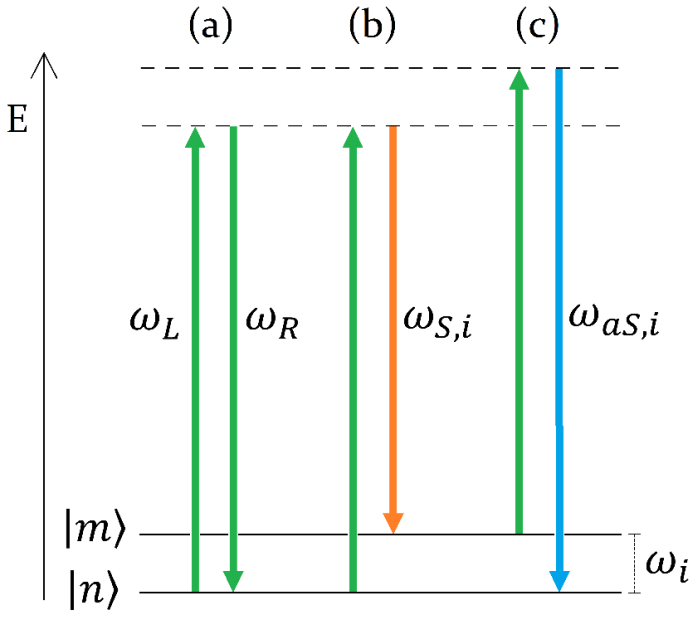

FIGURE 5. Scheme of (a) Rayleigh scattering (b) Stokes scattering (c) anti-Stokes scattering. $|n\rangle$ and $|m\rangle$ are vibrational states with quantum numbers $n = m \pm 1$. ω_R is the Rayleigh frequency, $\omega_i$is the frequency of vibration of the normal mode i and $\omega_{S,i}$ and $\omega_{aS,i}$ are frequencies of Stokes and anti-Stokes photons arising from interaction of excitation beam (ω_L) with vibrational mode i, respectively. The dashed line implies a virtual state.

to determine the number of layers and defects, in graphene samples and to see the extent and type of oxidation that has occurred.

1.2.2 Basic principles

There are two types of Raman scattering: Stokes and anti-Stokes. During the Raman proccess, the sample absorbs a photon, after which a photon is scattered from the sample to all directions. This scattered photon is observed in the Raman spectrum. The energy of this photon is discrete and depending on the Raman process the energy of this photon matches the difference between the initial photon and the energy of the excited vibrational state, of mode i, of electronic ground state (FIGURE 6). This is due to the quantization of energy of atomic scale vibrations.

$$\hbar\omega_{Raman,i} = \hbar\omega_L \pm \hbar\omega_i. \quad (2)$$

Here, the $\omega_{Raman,i}$, ω_L and ω_i are the frequencies of the Raman scattering, the excitation photon and the vibrational mode i, respectively. The negative sign in Eq. 3 stands for frequency of the Stokes scattering and the positive stands for anti-Stokes.

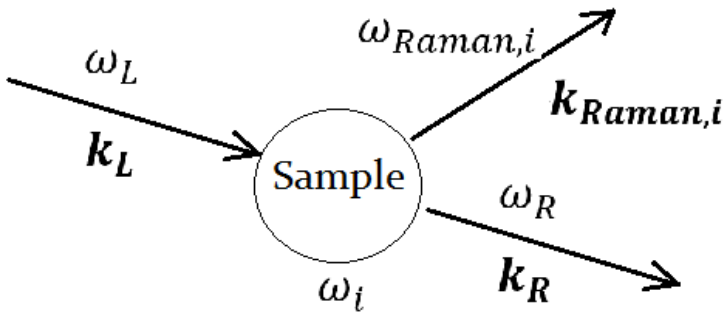

FIGURE 6. Description of Rayleigh (R) and Raman (Raman, i) scatterings, when the sample is exposed to electromagnetic wave, that is laser (L). In the image the, ω_L, ω_R and $\omega_{Raman,i}$, are the the frequencies of the excitation laser, the Rayleigh scattering and the Raman scattering arising from interaction with vibrational mode i (ω_i), respectively. $\boldsymbol{k_L}$, $\boldsymbol{k_R}$ and $\boldsymbol{k_{Raman,i}}$ are the corresponding photon wave-vectors associated to photon momentum.

The central concepts in Raman spectroscopy are induced dipole moment, $\boldsymbol{\mu}$, polarizability, α, and electric field, $\boldsymbol{E}$, and they are related as follows[89]:

$$\boldsymbol{\mu} = \alpha\boldsymbol{E} \quad (3)$$

Electric field (J/C), in this case, is the electromagnetic wave, which the system interacts with. Generally, a continuous wave laser beam is utilized and the wave can be represented by:

$$\boldsymbol{E} = E_0 \cos(\omega_L t) \tag{4}$$

Polarizability, α, is a material-dependent property. Polarizability links the electric field with the dipole moment. It is the change, $\alpha = \frac{d\mu}{dE}$, of generated dipole moment with change of surrounding electric field, and thus, a measure of how the dipole moment changes, when the material is exposed to electric field.
To evaluate polarizability, it is expanded to a Taylor series:

$$\alpha = \alpha_0 + \sum_i \left(\frac{\partial \alpha}{\partial Q_i}\right)_e Q_i + \sum_{i,j} \frac{1}{2}\left(\frac{\partial \alpha}{\partial Q_i \partial Q_j}\right)_e Q_i Q_j + \cdots \tag{5}$$

The vibration of the sample, with normal mode i, causes displacement, Q_i, on normal coordinates. The diplacement at low vibrational quantum states can be approximated as harmonic and it varies in time according to:

$$Q_i = Q_o \cos(\omega_i t), \tag{6}$$

Combining Eqs. (4), (5) and (6) with Eq (3), dipole moment becomes:

$$\boldsymbol{\mu} = \alpha_0 E_0 \cos(\omega_L t) + Q_0 E_0 \left(\frac{\partial \alpha}{\partial Q_i}\right)_e [\cos((\omega_L - \omega_i)t) + \cos((\omega_L + \omega_i)t)] \tag{7}$$

In Eq (7) the first term on the right side of the equation describes the Rayleigh scattering and the second and third terms represent Stokes and anti-Stokes, respectively. The Eq (7) also states, that if the change in the polarizability with the displacement of nuclei occurring during vibrational mode i is zero, that is if $\left(\frac{d\alpha}{dQ_i}\right) = 0$, the Raman scattering cannot occur. It should be noted that only one vibrational mode is considered and the second-order and higher terms in Eq (5) are left out.

The classical picture fails to explain the intensity ratio of Stokes and anti-Stokes scattering and it also cannot take into account the Raman selection rules. For this, a quantum mechanical representation is needed.

If $|n\rangle$ and $|m\rangle$ are orthonormal eigenvectors of transition dipole moment operator $\boldsymbol{\mu}$ and position (or displacement) operator $\boldsymbol{Q}$, the quantum mechanical treatment of Raman theory states:

$$|\boldsymbol{\mu}|_{\boldsymbol{nm}} = \langle n|\boldsymbol{\mu}|m\rangle = \langle n|\alpha|m\rangle \cdot \boldsymbol{E} = \left(\langle n|m\rangle \alpha_0 + \left(\frac{d\alpha}{d\boldsymbol{Q}}\right)\langle n|\boldsymbol{Q}|m\rangle\right) \cdot \boldsymbol{E}, \tag{8}$$

where $\langle n|m\rangle \alpha_0 \neq 0$, only if n = m, whereas presenting $\boldsymbol{Q}$ with creation and annihilation operators describing position, for harmonic oscillator:

$$\begin{aligned} |\boldsymbol{\mu}|_{\boldsymbol{nm,Raman}} &\propto \left(\frac{d\alpha}{d\boldsymbol{Q}}\right)\langle n|\boldsymbol{Q}|m\rangle = \left(\frac{d\alpha}{d\boldsymbol{Q}}\right)\langle n|(\boldsymbol{a}^+ + \boldsymbol{a})|m\rangle \\ &= \left(\frac{d\alpha}{d\boldsymbol{Q}}\right)\left(\sqrt{m+1}\langle n|m+1\rangle + \sqrt{m}\langle n|m-1\rangle\right), \end{aligned} \tag{9}$$

meaning, the Raman transition has non-zero probability if the transition occurs to state with vibrational quantum number, $n = m \pm 1$. As in classical representation, also in the quantum mechanical picture, $\left(\frac{d\alpha}{d\boldsymbol{Q}}\right)$ must be non-zero for Raman scattering to occur.

For solids, the fundamental Raman selection rule becomes[90]:

$$\boldsymbol{k_{Raman,i}} = \boldsymbol{k_L} \pm \boldsymbol{q_i}, \tag{10}$$

where $\boldsymbol{k_{Raman,i}}$ is the wave vector of the scattered photon, $\boldsymbol{k_L}$ is the wave vector of the incoming photon and $\boldsymbol{q_i}$ is the related quantity for scattered phonon of mode i. The positive and negative signs correspond to anti-Stokes and Stokes scattering, respectively. In first-order scattering, the fundamental Raman selection rule states, that because the wave-vector of photon $\boldsymbol{k_L}$ in visual wavelengths is significantly smaller than the phonon wave-vector, change induced to $\boldsymbol{q_i}$ by the photon is often negligible. Because of this, phonons with $\boldsymbol{q_i} \approx 0$ are observed.

The intensity of Raman signal can be ~1/100 of the Rayleigh scattering intensity. Since the Stokes signal has less energy than the excitation laser, fluorescence can overlap the entire Raman spectrum. Then, the anti-Stokes signal proves useful since it cannot be overlapped by fluorescence signals. However, the intensity of a Stokes signal, at room temperature, is usually significantly higher than an anti-Stokes signal, although this depends on the energy difference of ground and vibrational excited state and is therefore material dependent.

Raman scattering intensity is proportional to the fourth power of excitation laser frequency (ω_L^4) and directly proportional to the power of the excitation source. A Raman signal may be significantly improved by applying excitation energy similar to or the same as the energy difference between ground state and excited state of the material, corresponding to resonance Raman. This way, the signal intensity may be improved with two to three orders of magnitude.

1.2.3 Raman spectroscopy of Graphene

Due to the linear dispersion relation of the graphene band structure, energy difference between the ground state and the excited state, or the valence band and the conduction band, always matches the excitation frequency in the visible wavelength region, meaning that the resonance condition in Raman measurements is always met. Because of the strong signal due to the resonance-enhanced signal, Raman is very useful tool for characterization of graphene. The most important signatures for characterization of graphene are D, G, D′ and 2D-bands. A typical Raman spectrum of graphene is presented in FIGURE 7.

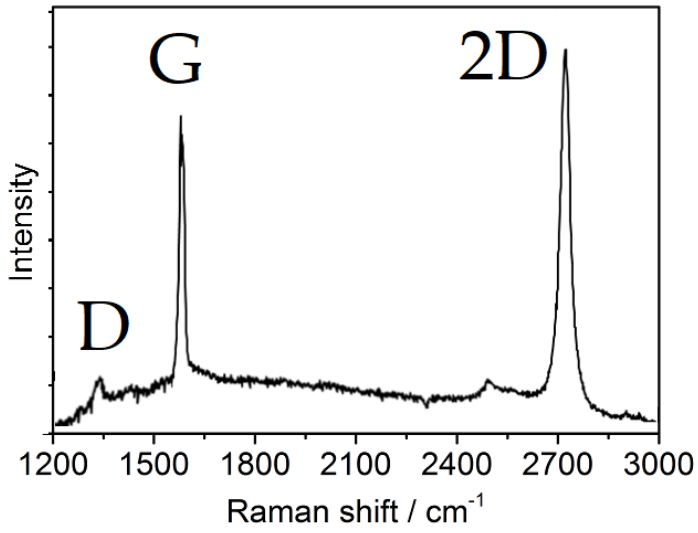

FIGURE 7. An example of the Raman spectrum of prisine graphene. The spectrum shows clear G-band and 2D-band. The defect bands D and D' are small or nonexsistent due to lack of defets.

G-band, or graphitic band, is present in all graphitic materials, such as single walled carbon nanotubes (SWNTs), fullerene, graphite and graphene and it represents the E_{2g} C-C in-plane stretching vibration.[91-95] For graphene, it can be considered as a measure of sp^2 carbons, and its central frequency exhibits wavenumbers ~1581 cm^{-1} – 1590 cm^{-1}, depending on number of layers, substrate, excitation laser power and defects.[6, 96-98] G-band exhibits a Lorentzian lineshape, which for undoped graphene has a central wavenumber at 1585 cm^{-1} and width of 7-16 cm^{-1}.[31] The G-band blueshifts and the width decreases with increasing doping. Interacting substrate causes an up-shift of the G-band compared to free-standing, suspended graphene.[99] Temperature has little effect on the width of the G-band but the band position is weakly temperature-dependent, with temperature coefficient -0.016 cm^{-1}/K.[100] Tensile strain causes a red-shift to the band position.[101] Thr G-band is a transverse optical phonon (TO) and the only major band together with the 2D-band in graphene permitted by Raman selection rules. All the Raman transitions of major bands of graphene are depicted in FIGURE 8.

D-band, represents a measure of defects in graphene. It originates from any defects breaking the in-plane symmetry, such as sp^3-defects, vacancies, boundaries and impurities. The D-band can be observed at ~1350 cm^{-1}. A narrow D-band points to well-defined types of defects, while a wider D-band implies amorphous structures. D-band exhibits a dispersive behavior with excitation energy and it is forbidden by selection rules, since $\boldsymbol{q_i} \neq 0$. However, since position of defects is well defined, they exhibit a broad momentum spectrum, by uncertainty principle. This momentum compensates the momentum required by the selection rule and enables the D Raman mode.[91]

Intensity ratio of D-band and G-band, I(D)/I(G) is a central concept when the point-defects of graphene are studied. In an experiment conducted by Lucchese et al., defects were induced on graphene with argon-ion bombardment, after which Raman spectrum of sample was measured.[102] They found that I(D)/I(G) increases as bombardment intensity is increased. These defects are thought of as point-like defects, and the distance between these defects, L_D, according to Lucchese *et al*. can be deduced from the I(D)/I(G):

$$\frac{I(D)}{I(G)} = \frac{102\ \mathrm{nm}^2}{{L_D}^2} \tag{11}$$

In Ar^+-bombarded graphene, defect densities up to ~10^{11} cm^{-2} still produced clearly defined Raman bands, whereas densities closer to 10^{14} cm^{-2} tended to blur the Raman spectrum, which ultimately resembles the spectrum of amorphous carbon.

D'-band, or longitudinal optical (LO) phonon, at ~1620 cm^{-1}, is another measure of defects in graphene. Both defect bands are forbidden by Raman selection rules. It has been suggested that the intensity ratio of D and D', I(D)/I(D'), can be applied to assign the nature of defects more specifically.[103] High I(D)/I(D') indicates sp^3-type defects, whereas moderate and low I(D)/I(D') points towards vacancies and boundary -type defects, respectively.

2D-band is a double resonant band observed around ~2680 cm^{-1} and it is also present in all graphitic materials. For graphene, the 2D-band is important for determining the number of layers in the sample. For single layer graphene, 2D-band scattering yields band shape of a single Lorentzian with width of ~30 cm^{-1}, whereas asymmetric 2D-band shape is a strong indication of multilayer graphene.[91]. Also, the intensity ratio I(2D)/I(G) is conventionally lower for multilayer than for single-layer materials, although, decreasing of I(2D)/I(G) indicates also elevated doping levels.[104] The position of 2D blueshifts with electron doping and redshifts with hole doping. Redshift of 2D-band may also be caused by tensile strain or rising temperature.[105]

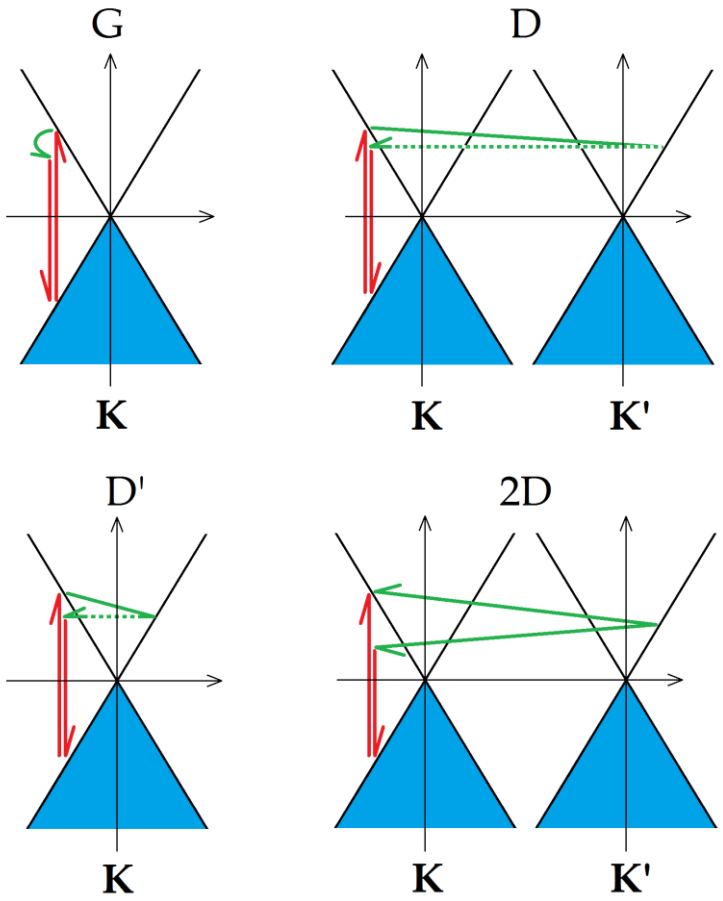

FIGURE 8. A presentation of Raman scattering processes of graphene. The blue color represents electrons, the red arrow represents transitions, the solid green arrow represents scattering, and the dotted green line represents scattering due to defects.

1.3 Ultrafast laser spectroscopy

In photography, when pictures of moving objects are obtained, the exposure time must be smaller than the time of the event, or the picture is blurred and the momentary information is lost. In ultrafast laser spectroscopy, pulsed lasers are used, where each pulse has a specific spectral and temporal width. On the analogy of photography, in ultrafast spectroscopy events are probed with pulses shorter than event duration. Movement of atoms during molecular vibrations, which occurs in 100 fs to 1 ps, is studied with femtosecond lasers.[106]

1.3.1 Coherent anti-Stokes Raman spectroscopy and Four-Wave Mixing

Non-linear optical spectroscopy is a set of delicate methods for studying the light-matter interactions of a material. There are several mechanisms for

non-linear light-matter interaction, generally referred to as multi-wave mixing processes. Converse to linear optical phenomena, optical nonlinearity is an intensity-dependent process and it is classified by order, which is determined by the number of photons involved in the process. Optical processes occurring in interaction between light and matter can be described by expansion of polarization:

$$\boldsymbol{P}(t) = \boldsymbol{P}^{(1)}(t) + \boldsymbol{P}^{(2)}(t) + \boldsymbol{P}^{(3)}(t) + \cdots \tag{12}$$

Linear processes ($\boldsymbol{P}^{(1)}(\boldsymbol{t})$), involve only one photon, $\boldsymbol{E}(t)$. The simplest nonlinear processes are three-wave mixing (TWM), or second-order nonlinear processes, $\boldsymbol{P}^{(2)}(t)$, involving two excitation photons. Third-order non-linear processes ($\boldsymbol{P}^{(3)}(t)$) involves interaction between three pulses. Classically:

$$\boldsymbol{P}(t) = \varepsilon_0 \chi E_i(t) + \varepsilon_0 \chi^{(2)} E_i(t) E_j(t) + \varepsilon_0 \chi^{(3)} E_i(t) E_j(t) E_k(t) + \cdots \tag{13}$$

Here, $E(t)$, is the electric field, $\chi^{(n)}$ is the n:th order optical response function, and ε_0 is the vacuum permittivity. Macroscopic electric polarization is defined as dipole moment per unit volume, and it takes into account the inhomogenous charge distribution of the medium. Microscopic description of polarization is dipole moment per molecule, or unit cell. In quantum mechanics, this is expressed as:

$$\boldsymbol{P}(t) = \langle \psi | \mu | \psi \rangle \tag{14}$$

With $|\psi\rangle = |\psi^{(0)}(t)\rangle + |\psi^{(1)}(t)\rangle + |\psi^{(2)}(t)\rangle + |\psi^{(3)}(t)\rangle$ ..., where (k) is the kth order perturbed wave function, yielding:

$$\boldsymbol{P}^{(k)}(t) = \begin{cases} \sum_{i=0}^{i<k} \langle \psi^{(i)} | \mu | \psi^{(k-i)} \rangle + cc., \text{for odd k} \\ \sum_{i=0}^{i<k} \langle \psi^{(i)} | \mu | \psi^{(k-i)} \rangle + cc. + \langle \psi^{(k/2)} | \mu | \psi^{(k/2)} \rangle, \text{for even k} \end{cases} \tag{15}$$

for kth order polarization.[107]

Generally, the higher-order signals exhibit lower intensity than lower-order signals. However, when non-linear signals are generated from materials with inversion symmetry, the second-order signals are cancelled out. In four-wave mixing (FWM) spectroscopy, three pulses, each possessing the same phase, are combined, in the same volume in a medium.[108] Thus all the beams must fulfill two overlapping conditions: temporal and spatial overlap, and the frequency of the generated FWM signal is governed by energy conservation law

$$\omega_l = \omega_i \pm \omega_j \pm \omega_k. \tag{16}$$

and the propagation direction is dictated by conservation of momentum

$$\boldsymbol{k_l} = \boldsymbol{k_i} \pm \boldsymbol{k_j} \pm \boldsymbol{k_k}. \quad (17)$$

When three fields, $E_1(t)$, $E_2(t)$ and $E_3(t)$, are combined in material and the overlapping conditions, energy and momentum conservations are met, the fourth field is generated in the process.

The generated signal has all the properties of a laser beam: the signal is directed, collimated, and coherent. Other signals are generated by all possible combinations of the excitation beams, with wave-vector governed signal directions, and they all represent different non-linear processes.

A sub-technique of FWM is coherent anti-Stokes Raman scattering (CARS) spectroscopy.[109] In CARS, the excitation beams ω_1, ω_2, and ω_3 are selected so that frequency difference of the first and the second interacting pulses, $\omega_1 - \omega_2$, corresponds to a Raman frequency, Ω, of a Raman active mode of the material. Pulses ω_1 and ω_2 are named here as pump and Stokes, respectively. Together, pump and Stokes generate a coherent state, which is then probed by the third beam (FIGURE 9a and 9b) The result is a CARS beam with frequency ω_4.

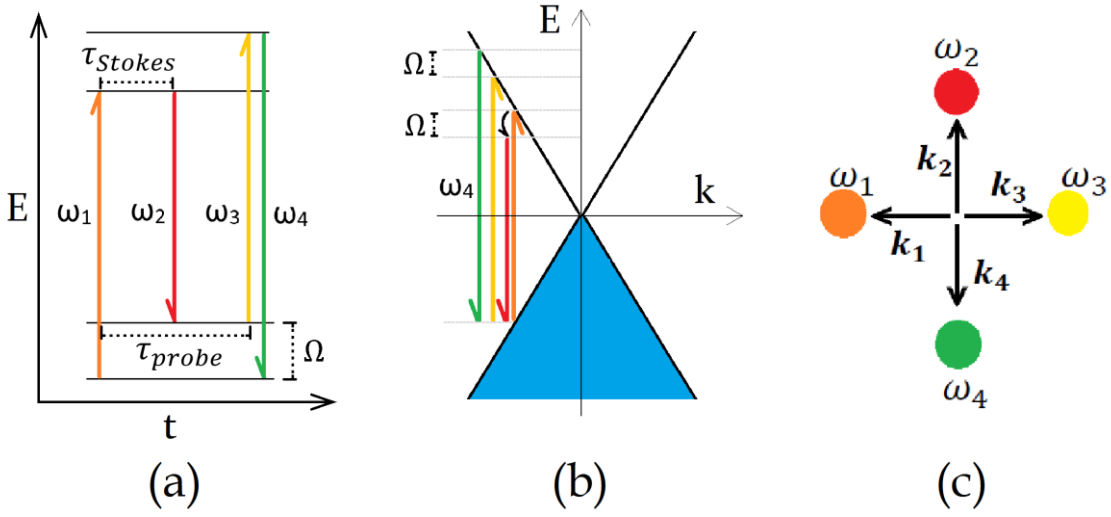

FIGURE 9. (a) Traditional energy diagram of CARS transitions. (b) Proposed corresponding transitions in graphene. (c) The wave vectors corresponding to beam propagation directions.

A common excitation geometry, is BOXCARS geometry (FIGURE 9c and 10). BOXCARS is convenient, since the separation of each involved field can be separated spatially and the combination signals can be easily characterized.

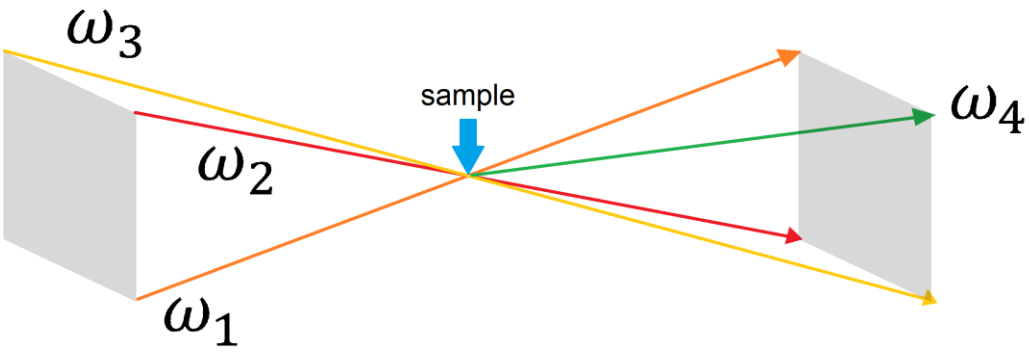

FIGURE 10. An illustration of BOXCARS excitation geometry. The beams ω_1, ω_2 and ω_3 propagate through sample and generate ω_4 while interacting in the sample medium.

Although CARS is experimentally complicated, it is an extremely powerful method in studying the coherent dynamics of Raman modes, because, the resonant CARS process produces a stronger signal than the non-resonant Raman signal, CARS signal, ω_4, has higher frequency than any of the excitation beams, meaning CARS will not be overlapped by fluorescence. Additionally, a material in any phase can be measured. Also, FWM-based techniques are useful for imaging the material if the third-order non-linear susceptibility is large and that for graphene $\chi^{(3)}$ is extremely large.[8]
FWM (and CARS) is especially useful for time-resolved experiments. When the beams fully overlap temporally, all possible combinations of FWM signals are

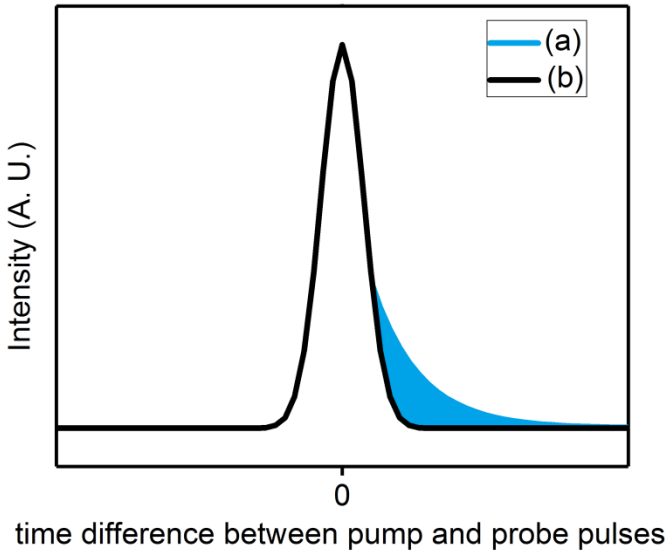

FIGURE 11. FWM signal intensity with respect to time difference of interaction of excitation and probing pulses. If a state with dephasing time persisting past excitation pulses is present, the intensity profile of the FWM signal is asymmetric (blue on positive side), whereas the lack of such signal only produces a Gaussian-like intensity distribution (black).

generated with maximum intensity. When interaction of one of the pulses is delayed with respect to others ($\Delta t \neq 0$), the signals arising from states with dephasing lifetimes following the Gaussian-like part may be seen (FIGURE 11). Thus, FWM provides a possibility to study coherent dynamics of a material.

1.3.2 FWM Microscopy

A combination of FWM (or CARS) signal and microscopy is a procedure, where a microscope image is constructed from an FWM signal. Two main procedures in microscopy are confocal imaging and wide-field imaging. In the former, the image is produced via point-by-point measurements, where the FWM (or CARS) signal is measured with a tight focus from a small spot and the FWM measurement is performed sequentially for each pixel of the image. In the latter, the imaged sample area is illuminated with a larger spot, where a FWM signal is generated, and the signal from the entire image area is collected with microscope objective.

The advantage of wide-field microscopy over confocal imaging (raster scanning) is that it is a single shot measurement, making it potentially very fast. Also, the single illumination of sample provides for the possibility of time-resolved imaging. A clear disadvantage of wide-field microscopy is the poor depth-resolution, although it is not an issue for two-dimensional materials.

Scanning FWM imaging has been performed on single-walled carbon nanotubes (SWCNT), where the energy difference between conduction and valence bands correspond to the excitation laser energy.[110,111] Such resonance effect enhances the signal intensity significantly. Indeed, CNTs where resonance condition is not achieved are difficult to detect with FWM imaging. However, for graphene the electronic resonance is always present due to the linear dispersion relation, which enables usage of a wide variety of excitation wavelengths.

Wide-field FWM measurements have been reported for other materials in the past.[112, 113] For graphene, third-order non-linear imaging using third harmonic generation (THG) and multiphoton absorption excited fluorescence (MAEF) have been shown to be rapid imaging methods.[114] With scanning method, fast FWM imaging of graphene was also reported recently.[115]

FWM imaging of graphene provides certain advantages over some existing techniques. Optical microscopy (OM) provides single step imaging and is widely used, and for characterization of number of layers, high resolution OM can be applied. But since the absorbance of visible wavelength in graphene is only 2.3%, observing < 0.5 μm-wide patterned structures is impractical.[27] Raman is a powerful technique for characterizing graphene; it is non-destructive and gives clear difference of the patterned structures and the layer structure; but Raman is also slow, the signal is relatively weak and in some cases possibly overlapped by fluorescence. Electron microscopy (SEM and TEM) and atomic force microscopy (AFM) provide high resolution and information about topography but these techniques are slow and inapplicable to observation of real-

time phenomena. Since the $\chi^{(3)}$ for graphene is large and the electronic resonance with excitation pulses is usually achieved, the FWM signals produced from graphene are strong and the excitation wavelengths for probing a state with frequency, Ω, may be chosen more freely.

1.3.3 Photodynamics of graphene

Time-dependent behavior of material can be uncovered in photodynamics experiments. Optical methods for investigating the dynamics vary with the purpose of the study, which can be the lifetime of an excited electronic or the vibrational state or dephasing of coherence.

When a molecule is photoexcited, the electron population is excited from ground state to excited state. The electronic transition occurs within attoseconds (10^{-18} s) and is considered instant in the scope of this thesis. Subsequently, the geometry of the excited compound relaxes to the energy minimum of the electronic excited state. Then, the population relaxes back to electronic ground state, via radiative transition directly (fluorescence) or indirectly by spin-orbit coupling (intersystem crossing, phosphoresence) or via non-radiative transition by coupling between vibrational states of electronic excited state and of ground state.

Each state in the relaxation process has a lifetime, and can in principle be investigated with light-matter interaction-related techniques. The lifetimes of different states for different materials vary within many orders of magnitude. An electronic excited singlet state of oxygen relaxing back to triplet ground state has a lifetime of > 70 minutes, whereas molecular vibrational states die out within 10^{-13} - 10^{-12} s.

Generally, linear optics can be utilized to probe lifetimes of long lived, radiative states and processes, via the observed emission. However, non-radiative transitions and ultrafast phenomena, such as vibrational relaxation and dephasing, must be studied with non-linear optical methods. Carrier relaxation in graphene occurs non-radiatively; therefore, studies of dynamics of graphene are carried out by non-linear methods.

In solids, discrete states are not distinguishable and the electronic excitation and relaxation cannot be discussed in terms of individual state populations. The excitation occurs to charge carrier (electron and hole) population in a certain energy range in the valence band. Second-order non-linear, two-photon, pump-probe-related experiments have uncovered the carrier relaxation processes in graphene, with help of theoretical investigations.[116, 117] For graphene, photoexcitation of electron population to conduction band causes chance in electron-hole distribution, which obeys Fermi-Dirac statistics at equilibrium (FIGURE 12a & 12b). Subsequently, the excited carrier population is thermalized via electron-electron scattering (FIGURE 12c). This gives rise to hot electron gas, which relaxes toward initial electron-hole distribution via electron-phonon scattering, simultaneously heating the lattice, until the equilibrium is achieved (FIGURE 12d). The electron-phonon scattering by optical phonons is

the dominating scattering procedure at room temperature. However, other relaxation phenomena, such as surface-plasmon resonance, along with the existence and behavior of excitons and Auger processes, have been investigated for graphene.[118-120] Different processes occur in different timescales and some of

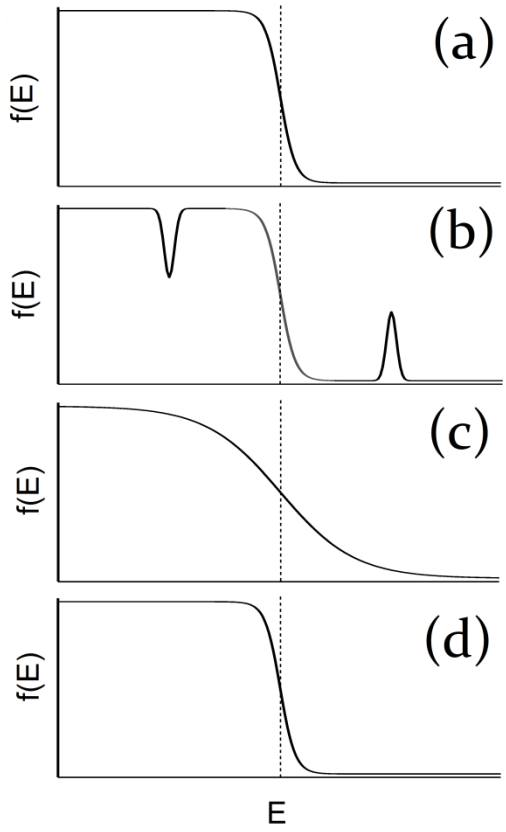

FIGURE 12. Schematic Fermi-Dirac carrier distribution of graphene (a) in equilibrium, before photoexitation (b) immediately after photoexcitation (c) after thermalization and (d) after carrier relaxation via electron-phonon scattering. Fermi level is marked with a dashed line.

them are competitive. The electron-electron scattering occurs within < 200 fs.[116, 121] Also, Auger scattering take place in < 200 fs.[122] The electron-phonon scattering for optical phonons is known to dominate at room temperature and it usually begins at ~ 200 fs and is in quasi-equilibrium with electron-electron scattering. Also, electron-optical phonon scattering has been shown to depend on the defect density.[115] The electron-acoustic phonon scattering occurs in order of picoseconds, depending on the temperature.[123]

The second-order methods rely on observation of population, whereas third-order polarization, according to Eq. 15.

$$\boldsymbol{P}^{(3)}(t) = \langle \psi^{(0)}(t) | \mu | \psi^{(3)}(t) \rangle + \langle \psi^{(1)}(t) | \mu | \psi^{(2)}(t) \rangle + cc. \qquad (18)$$

contains information on the time-evolution of coherences of the system, or more precisely time evolution of the overlap between wave functions in different quantum states. The first term on the right side of th equation (and its complex

conjugate) is responsible for the CARS process, which is an excellent tool for studying phonon dynamics.

1.3.4 Photo-oxidation of graphene

Photo-oxidation is a photochemical process where an oxidation reaction is induced with light. Oxidation refers either to removal of electrons, removal of hydrogen or addition of oxygen to the system. Structure of major oxygen containing groups in GO (-OH, C-O-C, and COOH), indicates that graphene is oxidized by addition of oxygen containing groups to sp^2 carbons of graphene changing their hybridization to sp^3.

Photo-oxidation of graphene has been performed by utilizing UV-wavelength continuous wave (CW) laser with in presence of ozone.[85] However, with the UV/ozone method patterning is relatively time-consuming and also involves usage of ozone, which is considered toxic.[124] Moreover, CW visible wavelength laser patterning studies showed that oxidizing graphene by such a method takes several hours and thus is most likely achieved by heating.[105] Also, oxidation of graphene has been done with pulsed laser by applying visible wavelengths.[125]

It was observed in pulsed oxidation experiments, that with pulse duration of 280 fs, the oxidation follows second-order non-linear kinetics.[125] Raman measurement of the graphene sample after pulsed oxidation showed significant increase of I(D)/I(G) relative to non-patterned graphene. Also, with patterning of graphene with femtosecond laser pulses above a specific intensity limit, ablation of graphene is induced. Indeed, in graphene oxide the "defects" are merely added oxygen-containing functional groups on graphene, causing local changes on the periodic sp^2-carbon membrane, shown in the Raman spectrum as defects.

2 EXPERIMENTAL METHODS

2.1 Raman spectroscopy

A home-built Raman setup was used for all Raman measurements and imaging. Backscattering geometry with 532-nm excitation wavelength produced with CW single-frequency laser (Alphalas, Monolas-532-100-SM) was applied. The beam was focused, and then collected, with a 100x microscope objective (Olympus 100x with 0.70 N.A.). Acton, SpectraPro 2500i 0.5 m spectrograph was utilized to disperse the scattered light and direct it to an EMCCD camera (Andor Newton EM DU971N-BV). The 80-µm slit width was utilized in all measurements, except that the suspended samples were measured using a 100-µm slit. The measurement point was observed visually by applying a beam splitter between the objective and the spectrometer. The Rayleigh scattering was attenuated with an edge–filter (Semrock). In most cases, the sample movement was controlled with a XYZ-piezoscanner (Attocube, ANPxyz101) with smallest step of 50 nm. However, in Paper III the sample was moved with ThorLabs, Nanomax 300 piezo stage. Usually, laser powers of 1-1.5 mW were utilized except in Paper I, where ~5 mW power was used.

2.2 Wide-field femtosecond FWM microscopy

The core setup for FWM widefield experiments is described in FIGURE 13. FWM imaging was conducted by producing three laser pulses with three home-built non-collinear optical parametric amplifiers (NOPAs). For each beam, the fundamental beam (Coherent Libra – S, 1 kHz, 1 mJ, 800 nm) was split in two, the 800 nm was utilized as a seed pulse and the other part was frequency-doubled and used as a pump in NOPA. The three beams (610, 670, and 585 nm), corresponding to pump, Stokes and probe, were utilized to produce the FWM signal. Prism compressor pairs (SF10) were used to compensate the group ve-

locity dispersion, resulting in pulses with durations of less than 55 fs. The beams were focused on the same spot and the temporal overlap was achieved with optics and optical delay stages. The resulting FWM wavelength was 539 nm with Stokes shift at 1468 cm^{-1} with the intention of overlapping with the energies of the D- (1350 cm^{-1}) and G-bands (1585 cm^{-1}) of graphene. The signal mainly originated from electronic response. Beam fluences were controlled with neutral density filters. Excitation beams were focused on the sample in the BOXCARS geometry.

The sample was attached on manual XYZ – translation stage for controlled movement of the sample. Diameter of the irradiated area was 50 µm and the FWM signal was collected by a microscope objective (Nikon LU Plan 50x/0.55). The signal was filtered from the other beams with two bandpass filters (Semrock FF02-531/22-25 and FF01-531/40-25 at λ = 531 ± 11 and 531 ± 22 nm, respectively). Finally, the image was focused on an EMCCD camera (Andor Newton EM DU971N-BV) with a lens (f = 200 mm) that was installed behind the objective.

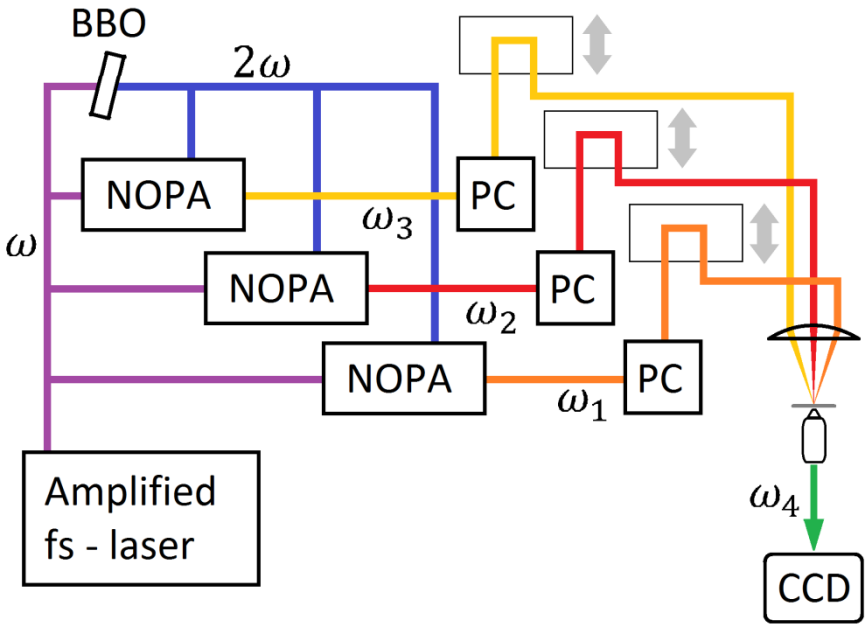

FIGURE 13 Schematic view of the setup utilized in original papers I and V. NOPA = non-collinear parametric amplifier, BBO = β-$Ba(BO)_2$ crystal, PC = prism compressor, CCD = charge coupled device – detector. The boxes with gray arrows on their right represent delay lines of signals.

2.3 Graphene photo-oxidation

2.3.1 Oxidation patterns.

A femtosecond laser (Pharos-10, R = 600 kHz) was utilized for pumping NOPAs (Orpheus-N, Light Conversion) to produce the beams utilized for two-photon direct writing and scanning of samples with FWM microscopy imaging. The pulses were compressed with a fused silica prism pair, to a temporal width of 40 fs, and subsequently directed to the sample through microscope objective (Nikon LU Plan ELWD 100×/0.80). Time delay between the two beams was controlled with delay lines (ThorLabs), to achieve temporal overlap between pulses. The photo-oxidation was performed under ambient conditions, whereas the imaging was done under nitrogen purge, and the sample was moved during the processes with piezoelectric stage (ThorLabs), with 100-nm step size. Finally, the FWM signal generated in imaging was detected in backscattering geometry with optical filtering and single photon avalanche photodiode (SPCM-AQRH-14, Excelitas Technologies).

In Paper I the suspended single layer graphene was oxidized using λ = 540 nm and intensity range 10^{11}-10^{12} W/cm^2. Intensity range utilized for imaging was $5 \cdot 10^{10}$-$2 \cdot 10^{11}$ W/cm^2. Single point was irradiated typically 0.1-0.2 s and the step size between points was 100 nm.

Sixteen different pulse energy and irradiation times were utilized in Paper II. 8.3, 10.5, 13.3 and 16.6 pJ and for each, irradiation times 0.2, 0.5, 1.0, 2.0 s/spot was applied. Each combination was utilized to pattern 5 x 5 matrix of spots (width ~400 nm) with 1 µm spacing. For imaging, 3 pJ pulse energy was applied.

In Paper III, 2 × 2 µm^2 squares were patterned on single layer graphene on Si/SiO_2 substrate by using 13 pJ pulse energy and changing the irradiation time / spot for each square. Eight squares were patterned with oxidation times 0.1, 0.2, 0.3, 0.4, 0.5, 0.6, 0.8, and 1.0 s/spot. Each square was patterned five times, resulting in an 8 x 5 matrix of patterned squares, with 2-µm spacings. For imaging, 3 pJ pulse energy was applied.

In Paper IV, the oxidation beam was directed to sample through a microscope objective on the imaging setup and the detection site of the imaging setup was modified by installing an additional 45° dichroic long-pass filter (FF552-Di02-25x36 corresponding to transmission for λ > 552 nm) between the detector and objective and changing the detector position accordingly. The wavelength of the oxidation beam was 590 nm and the oxidation and ablation patterns were formed by moving the oxidation beam manually with a mirror (FIGURE 14).

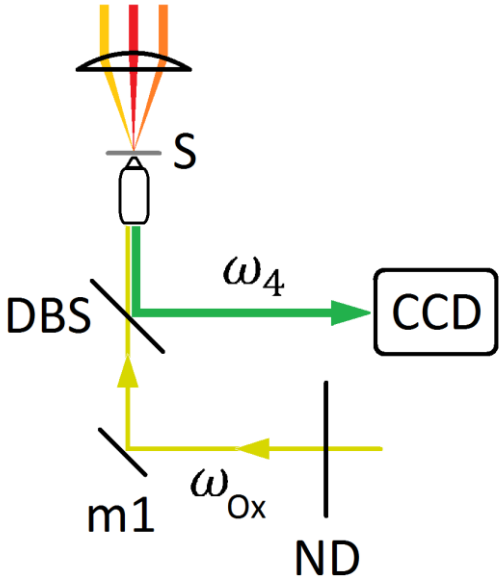

FIGURE 14. The detection site of setup utilized in the real-time following of photo-oxidation experiment. DBS = Dicroic beam splitter (45°), S = sample, m1 = mirror, ND = neutral density filter.

2.4 Time-resolved coherent anti-Stokes Raman measurements

Time-resolved CARS measurements were conducted by fixing a delay line of ω_1 and varying time delay of ω_2 and ω_3 separately (FIGURE 13). All the possible beam combinations of the excitation beams produce a CARS signal probing a different coherent Raman process. Each CARS signal has a different central wavelength and direction governed by the phase-matching conditions. By using BOXCARS approach, CARS signals originating from different non-linear processes were separated and assigned, unequivocally. The signals were collected by focusing the generated signals on camera and filtering out the excitation beams. A signal pattern resembling the pattern showing ω_4', ω_4'', ω_4''' and ω_4 is shown in FIGURE 15a. Signals ω_4', ω_4'' and ω_4''' are resulted from two-pulse in-

teractions i.e. $\omega_4' = 2\omega_2 - \omega_3$, and ω_4 from three-pulse interaction ($\omega_4 = \omega_3 + \omega_1 - \omega_2$).

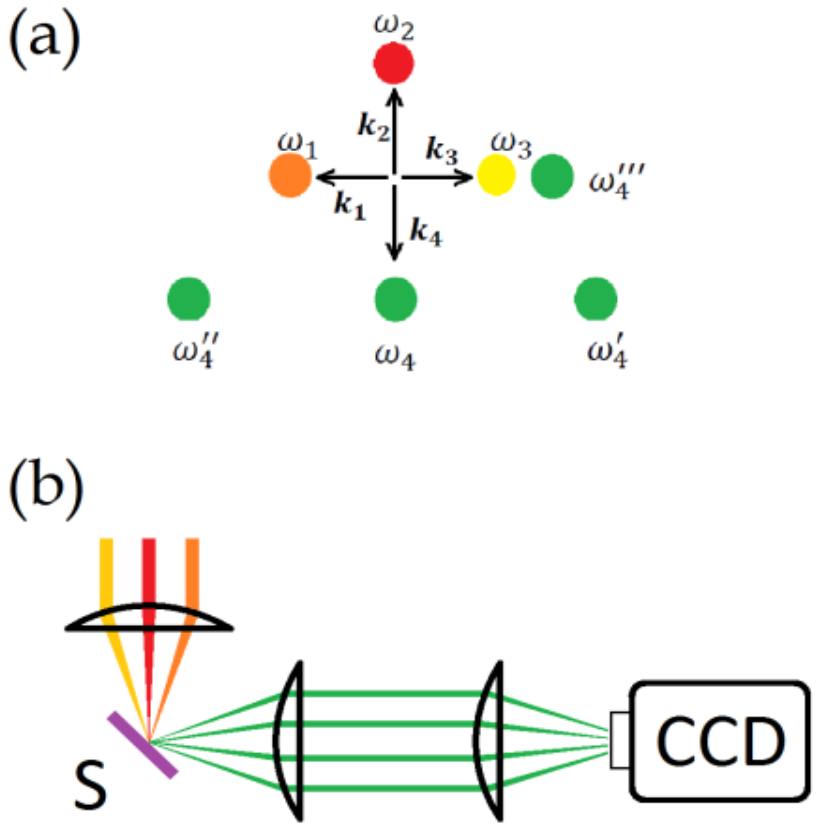

FIGURE 15. (a) Depiction of all the CARS beam contributions seen in dephasing phonon measurements. Positions of the green signals are governed by the wave vectors. (b) The detection site of setup utilized in the coherent dynamics measurement.

The excitation signals were directed to a detector with two consecutive lenses instead of passing on a collimated signal with microscope objective and the detection was performed with Q-IMAGING, Retiga R1, CCD imaging camera.

3 RESULTS AND DISCUSSION

3.1 Structure and optical properties of untreated graphene

3.1.1 Raman and chemical composition

Raman spectroscopy was used for characterization of graphene, revealing the number of layers and the quality, in terms of number and nature of defects. Micro-X-ray photoelectron spectroscopy (μ-XPS) was used for chemical composition measurements.

Raman spectrum measured from graphene on Si/SiO_2 surface (FIGURE 16a), concludes that the sample contains single layer graphene with only minor amounts of defects. The G-band was found at ~1590 cm^{-1} and the bandwidth was ~11 cm^{-1}. Single Lorentzian function describes perfectly the intensity distribution of the band. The bandwidth is in accordance with the literature but the position is slightly blue-shifted compared to what has been shown for non-doped graphene.[31] The increased G-band frequency is not an unusual situation as moisture is known to support physisorption of oxygen molecules on graphene surface, which induces electrostatic doping.[126] Also, the G-band can be stiffened due to slightly increased defect density.[98]

The position (~1365 cm^{-1}) and width (~20 – 30 cm^{-1}) of D-band are in accordance with previous reports.[91, 127] Unlike G-band, the single Lorentzian is not an ideal description of D-band distribution. The accurate quantitative analysis of the band using function fitting results in high relative errors. However, sufficient estimation of the D-band height for I(D)/I(G) can be done, as the main purpose is to see changes in I(D)/I(G). Intensity ratio of D-band and G-band for single layer graphene is ~ 0.1, which relates to defect density of ~10^{11} cm^{-2}.[102] The shape and width of D-band are also important but become more visible when defects are induced on graphene.

The 2D-band fits perfectly to one Lorentzian, which along with the 2D and G-band intensity ratio, I(2D)/I(G) > 1, is conclusive evidence for single layer

material.[98] The band position is at ~2690 cm^{-1} and the width ~30-40 cm^{-1}, which both match reasonably well the earlier reported values.[98]

Also, an air-suspended graphene sample was characterized. The suspended sample was needed to test if the two-photon oxidation patterning is ablative or non-destructive. Raman spectra measured on an air-suspended single layer graphene has only minor differences to corresponding spectra measured on samples on substrate. The D-band is smaller compared to graphene sample on substrate, indicating the absence of electrostatic interaction with the substrate.[97]

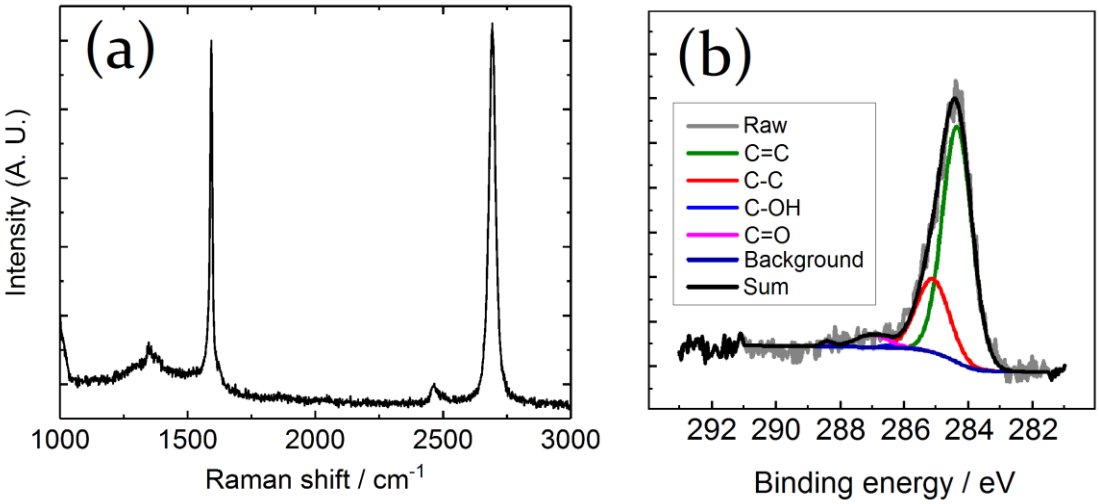

FIGURE 16. (a) Raman and (b) μ-XPS spectrum of single layer graphene on Si/SiO_2 substrate.

The difference can be seen as a broad baseline under D-band in Raman spectrum in FIGURE 16a. The G-band is found at lower frequency (~1589 cm^{-1}), which can be expected for air-suspended single layer graphene due to the lack of interacting substrate.[99]

The chemical compositions of the investigated samples were obtained with μ-XPS. In XPS, the sample is irradiated with X-rays. The energy of the X-ray photon is absorbed by some lower core valence electron which is ejected from one of the atoms in the sample. The kinetic energy of the emitted electron is acquired, and since the photon energy of the X-ray is known, the binding energy of the emitted electron can be calculated. The XPS spectrum is then constructed as intensity of the emitted electrons as a function of binding energy. For a different chemical environment, the binding energy is unique, which makes XPS extremely useful for chemical composition measurements. In μ-XPS the, X-ray beam is focused on the sample with Fresnel zone-plane optics, to achieve high spatial resolution. μ-XPS spectrum shows the chemical composition of graphene on the Si/SiO_2 substrate (FIGURE 16b). Approximately 95 ± 5 % of the sample is composed of C-C and C=C, shown in the spectrum as Gaussian distributions with maxima at 285.0 eV and 284.4 eV, respectively.

3.2 Photo-oxidation

Locally controlled, tunable bandgap opening of graphene is needed to produce graphene-based electronics. For this, two-photon oxidation patterning with fs-laser is a suitable method. However, the structure and properties of the patterns fabricated using the method must be further investigated.
The patterned features were investigated with Raman, XPS, FWM and AFM, the results were compared to non-modified graphene and related to each other.

3.2.1 Photo-oxidation of air-suspended graphene

Scanning FWM images were recorded to see the spatial changes of the FMW signal and to compare the image with results obtained from Raman.

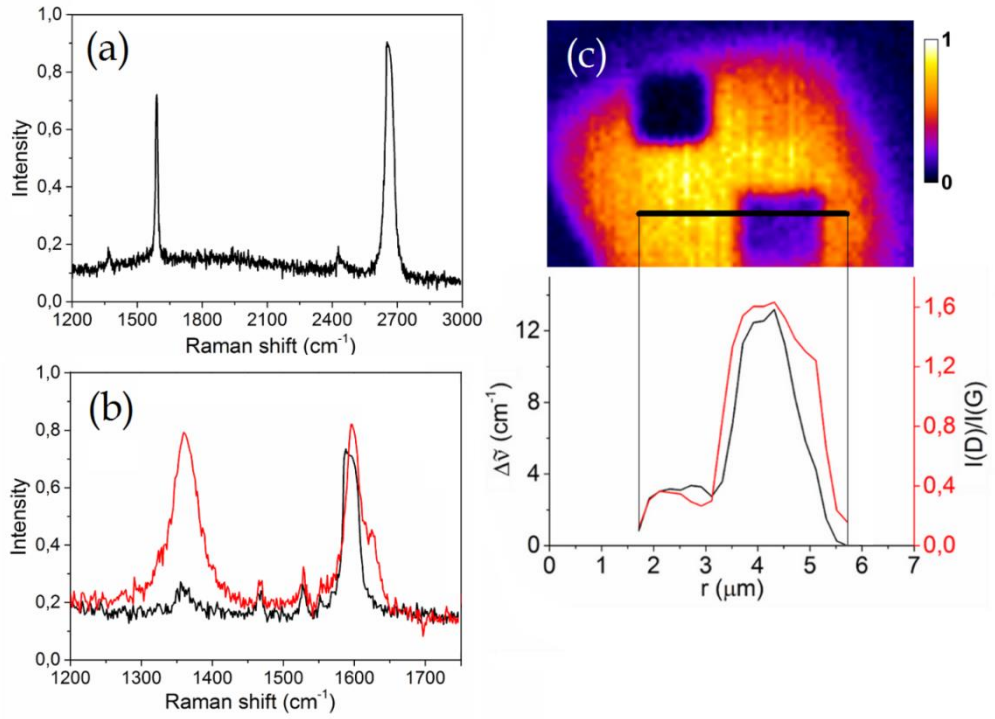

FIGURE 17 (a) Raman spectrum of a suspended single layer graphene. (b) Raman spectra of D and G-band region of graphene before (black), and after (red) oxidation. (c) Scanning FWM image of a patterned 7 x 7 μm² opening with 2 x 2 μm² patterned structure and a Raman cross-section of the pattern showing significant change in I(D)/I(G) and G-band position in the oxidized area. (Paper I)

A solid square (2 x 2 μm²) was patterned on an air-suspended single layer graphene and Raman spectra were measured from oxidized and non-oxidized regions (FIGURE 17). The ratio I(D)/I(G) and the G-band frequency were determined. The changes in the Raman spectra are similar to corresponding changes between pristine graphite and graphite oxide.[128] The fact that the Raman spec-

trum could be obtained from the patterned structure affirms the fact that the oxidation process is non-destructive and ablation does not take place.
FWM raster scanning imaging showed almost complete diminishing of the FWM signal intensity in the locations where the patterning was performed. Such a clear change in the FWM signal without damaging the material indicates a change in the electronic structure of the material. Also, the rate at which the oxidation occurs was concluded to follow second-order kinetics, which indicates that the photo-oxidation is a two-photon process.

3.2.2 Effects of photo-oxidation on graphene surface topography

The oxidation patterning was proven functional with air-suspended graphene but to obtain information on the topography of the oxidized patterns graphene samples on a Si/SiO_2 substrate were used together with AFM imaging. In the oxidation process, two parameters were varied, pulse energy, E and irradiation time, t. These values were used to calculate the irradiation dose (E^2t), which was related to the AFM results. The fabricated sample was a matrix of spot-like patterns patterned with different doses.

In AFM, the sample surface is scanned with a mechanical probe and the force that is inflicted from the sample to the tip is measured, and the image is constructed as a function of surface height. The AFM measurements of patterned structures on the surface of a graphene show a 400 nm-wide spot with height increased 1-2 nm above the graphene surface surrounded by ~50 nm wide "cleaned" areas. More close examination of the irradiated areas reveals that the patterned structures are not homogenous, but are constructed from small "islands". Even the exposure to the smallest dose shows that the roughness of the surface is flattened and several grain-like features have formed within the irradiated area (FIGURE 18b). The unpatterned surface outside patterned features is rough. This roughness is caused by polymer residuals originating from the transfer process of graphene.

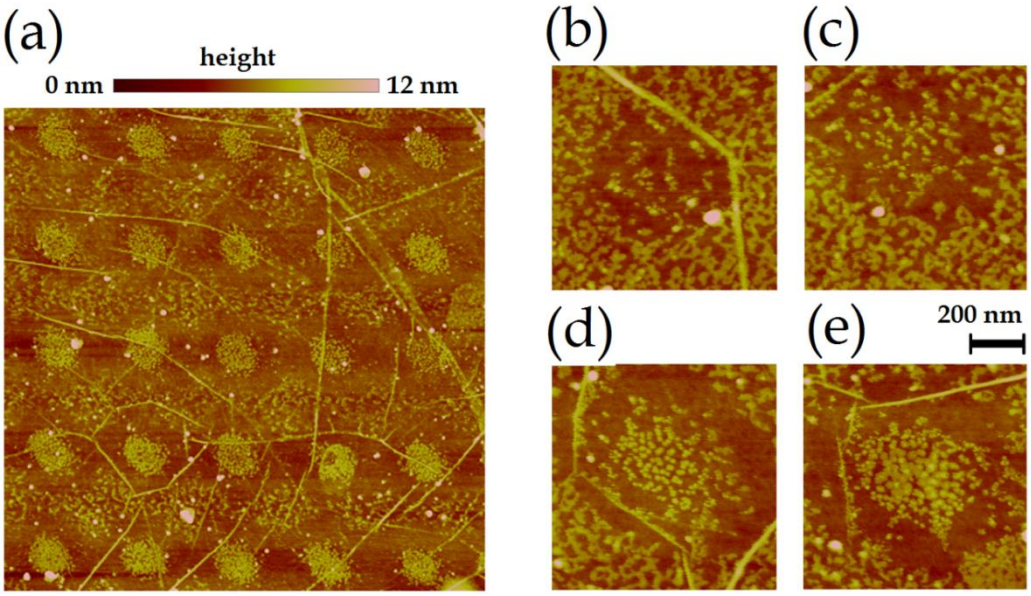

FIGURE 18. Atomic force microscopy images of patterned spots with different irradiation doses. The entire sample consisted of a 4 x 4 matrix of 5 x 5 patterns shown in (a). Each of the spots in 5 x 5 matrix were patterned using the same irradiation time and pulse energy, which in patterns in (a) are 16.6 pJ and 1s. In (b), (c), (d) and (e) the pulse energy was 8.3 pJ and the patterning time / spot was 0.2, 0.5, 1.0 and 2.0 s, respectively. It is clear the original roughness is "cleaned" and the patterns are evolved from seed-like expanding grains.

The new islands are formed and existing islands grow when the dose is increased. As the island width reaches 30 to 40 nm, the islands merge with adjacent islands (FIGURE 18 b-e), which is when the total area of islands within the oxidized area saturates it (at ~200 $(pJ)^2s$). The island formation and growth is depicted schematically in FIGURE 19.

A phenomenological simulation model was constructed to obtain more knowledge about the island formation and island growth. The model is a variant of the Eden growth model and it provides insight on the ratio of probability of forming new oxidation site on pristine graphene to probability of forming a oxidation site at an edge of an existing island, p_p/p_e, and the growth kinematics.[129] By fitting the model to the results it can be concluded that there is a 10^5 higher probability of generating a site as an extension of an existing island than of generating a new island. This leads to a fact that the proportion of smaller islands is larger with lower doses, whereas the larger islands dominate at higher doses.

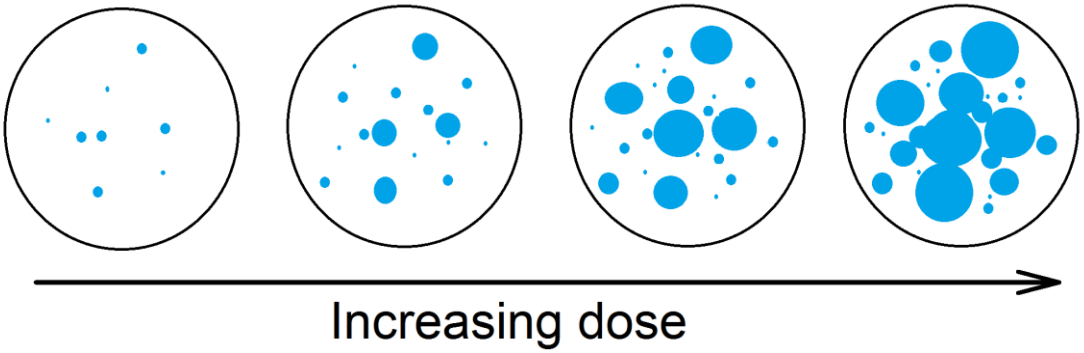

FIGURE 19. Schematic representation of island (blue) growth with increasing dose in the patterned 400-nm spot-like area (black circle).

The results obtained by AFM provide a top-down approach for investigation of the mechanism of the two-photon oxidation on a molecular level. It remains to be seen in the future if the reaction is initiated from point-like sources also in atomic scale. Tackling the atomic scale mechanism could uncover a new approach to functionalize graphene with different chemical groups. The AFM and the phenomenological model offered a macroscopic description of the formation of the patterns. However, the lateral resolution of the AFM (8 nm) utilized in our experiments sets limits to the measurements and the processes inside the islands must be investigated using other methods, such as scanning tunneling microscope (STM).

3.2.3 Defect density and a peek inside the islands

As the photon dose increases, the islands grow and the distances between the induced defects fall below the lateral resolution limit of AFM. At this stage, Raman is able to provide useful information on the changes induced by oxidation patterning. The insight about chemical changes inside the islands is a key element towards understanding photo-chemistry between graphene and oxygen.

The width, position, intensity and shape of the main Raman bands G, D and 2D were followed with different irradiation doses. In general, I(D)/I(G) provides the distances between the defects, peak positions indicate changes in doping or

electronic structure and band widths describe if the material is well-defined or amorphous. The scanning FWM and Raman I(D)/I(G) images of the oxidized sample are presented in FIGURE 20. The FWM image shows gradual decrease of the signal intensity with increasing dose. The changes in Raman spectra associated with the oxidation process are not visible until 140 $(pJ)^2$, where the G-band width decreases but eventually returns to its initial value at higher doses. When patterning is performed with doses, at which the island growth reaches saturation, the G-band up-shifts and 2D-band down-shifts and narrows compared to graphene. Before the oxidation the sample is p-type doped, due to adsorbed oxygen and water molecules. This doping is further enhanced due to progressive oxidation, which results in frequency shift of Raman bands. Single Lorentzian fit to G-band data was not validated after the oxidation, as the increasing D'-band deformed the shape of G-band.

The results show an increase in I(D)/I(G) with rising irradiation dose saturating at the same dose at which the islands merge. The I(D)/I(G) never reaches higher values than 0.4, corresponding to defect density of $\sim 4*10^{11}$ cm^{-2}.[102] This is significantly lower than would be expected, based on the patterning experiment conducted on air-suspended graphene. However, the Raman spot size exceeds the size of the patterned structures and thus the spectrum of graphene dilutes the observed spectra. The actual I(D)/I(G) was evaluated by treating the observed spectrum as a linear combination of oxidized and pristine graphene under the Raman spot. After the evaluation, I(D)/I(G) maximum reached ~0.8 which corresponds to defect density 10^{-12} cm^{-2}.[102]

When only a few oxygen-containing functional groups are added covalently on graphene, the material can be thought of as doped graphene. However, when an atom or a functional group is added to a material covalently the chemical structure and the electronic structure of the material is changed. Truly, it is known that band structure of GO differs from band structure of graphene as GO has an existing bandgap while graphene does not. This raises an interesting question: To what extent can the changes in Raman spectra be explained by doping effects and at what point of the oxidation can one denote the material as GO?

These experiments showed that Raman is a useful tool for acquiring atomic scale insight about the oxidized structures. The oxidation patterning induces sp^3-type defects (D-band) which are well-defined even with the higher doses. The I(D)/I(G) saturates where the island merge. This uncovers an approach to the initial steps of the mechanism of the oxidation: the oxygen attaches to sp^2-type sites of graphene giving rise to sp^3-hybridized carbons. Raman also provides versatile information about the possible doping and strain effects involved in the process but the actual chemical groups distorting the periodic structure of graphene must be clarified with XPS.

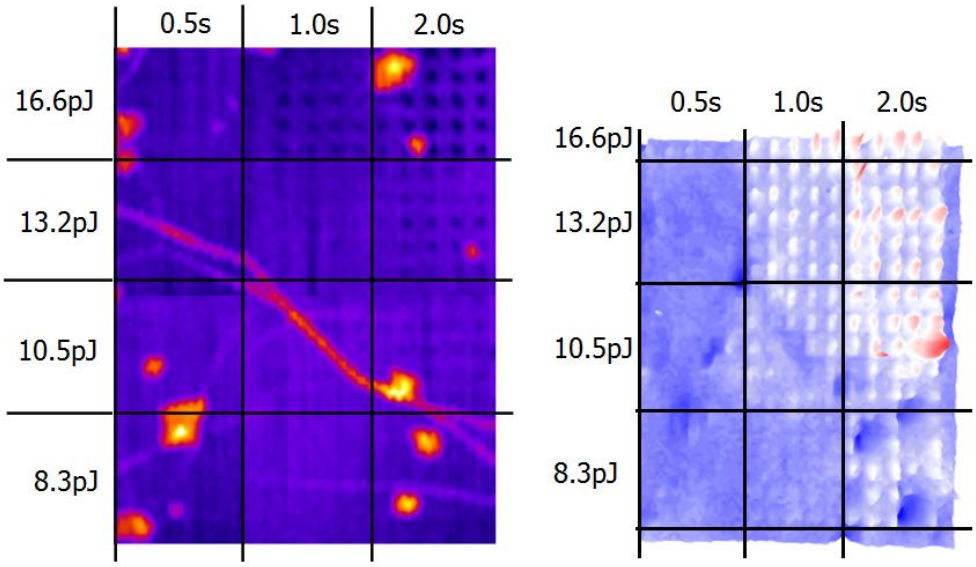

FIGURE 20. Scanning FWM (left) and Raman I(D)/I(G) (right) maps of twelve of the sixteen areas, each patterned with different irradiation times and pulse energies. The four areas patterned with 0.2 s irradiation times are left out since they did not show any detectable changes in the Raman spectra or the FWM image.

3.2.4 Chemical composition on patterned areas and another peek inside the islands

To gain insight into the chemical composition of two-photon oxidation patterns, graphene on Si/SiO_2 substrate was studied with μ-XPS. The results were compared to the chemical composition of graphene and related to Raman spectra of the patterns (FIGURE 21a). Several square-shaped features with different doses were patterned and the patterns were also made large enough that the Raman spectrum would not be diluted by surrounding graphene. The same patterns were also imaged with raster scanning FWM microscope (FIGURE 21b).

As the dose increases, the proportions of C-C and C=C in graphene decrease and the proportion of hydroxyl (-OH) and epoxide (C-O-C) groups are increasing with increasing irradiation time. At the first oxidation step, the dramatic changes in the chemical structure of patterns are not observed, but eventually proportion of the hydroxyl group increases drastically. In the end, only ~35 % of the material is composed of graphene-like carbon, while proportions of hydroxyl and epoxide groups dominate the majority of the structure.

In Raman measurements, the I(D)/I(G) increases only slightly at the initial

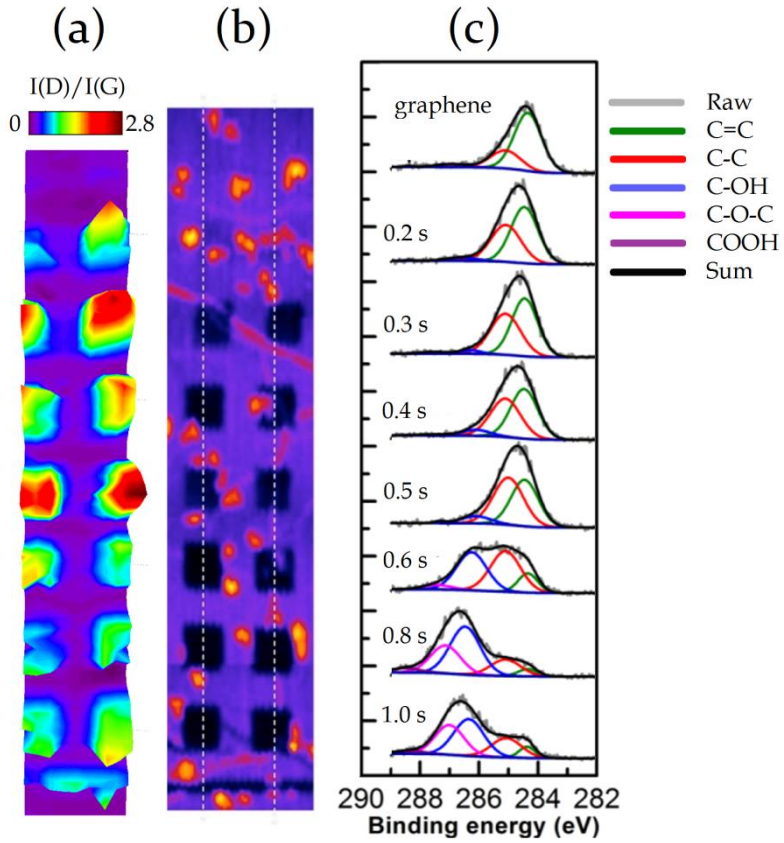

FIGURE 21. (a) I(D)/I(G) Raman map (b) scanning FWM image (c) XPS spectra of the set of oxidized 2 x 2 μm^2 square patterns.

step but reaches 2.8, which corresponds to defect density ~10^{13} cm^{-2} at 0.5 s irradiation time.[102] Here, the D-band still remains well defined and throughout the process the bands remain narrow compared to chemically produced GO.[84, 130] The point, where a notable decrease in sp^2 carbons occurs in the XPS spectrum (at 0.6 s in FIGURE 21c) corresponds to a point at which the material according to the Raman spectra begins to degrade.

Because the maximum of I(D)/I(G) corresponds to L_D ~ 11 nm, which is close to the utilized lateral resolution of AFM (8 nm), Raman proves extremely useful in investigation of chemical structure inside the formed islands. Results of the Raman study can be directly related to the XPS-spectra. The initial change of I(D)/I(G) is related to the observed change in proportional carbon hybridization between sp^2 and sp^3 in XPS. XPS and Raman measurements together provide new insight into the process and an approach to formulating the oxidation

mechanism at molecular level: The oxidation begins with functionalization of adsorbed oxygen, possibly assisted by water molecules. Mainly, the oxidation progresses around the point-like sources, forming islands, which eventually coalesce. Before merging, the defect density is relatively low, but as the island diameters reach ~30 nm (0.5 - 0.6 s), the degree of oxidation increases, eventually resulting in a final product with 40% hydroxyl, 25% epoxide, and a few percent of carboxyl groups, with respect to graphene content.

3.3 Characterization of graphene with femtosecond laser pulses

3.3.1 Wide-field FWM imaging

The patterning of graphene entails the need for a fast characterization method. That is, to reliably fabricate graphene-based devices the patterning needs to follow the patterning in real-time. A method fulfilling this need was developed utilizing the exceptionally large third-order non-linear optical response of graphene combined with advantages of wide-field microscope imaging resulting in FWM wide-field imaging.

The strength of the method was demonstrated for characterization of suspended graphene. The sample was a TEM copper grid with 7 x 7 μm^2 openings, which was covered with single layer graphene, leaving graphene hanging on air where the openings were located. The suspended single-layer graphene covering several windows was patterned with recognizable patterns. The patterns were imaged with scanning FWM for comparison.

In the oxidized parts, the FWM image showed almost complete reduction of the FWM signal intensity in oxidized features. Also, the FWM signal arose from broken or half-covered windows, showing only on the parts where graphene existed. Additionally, the grains and possible local multilayer parts were observed as brighter spots. An optical microscopy image was not able to reproduce features observed in an FWM image, but showed linear transmission from

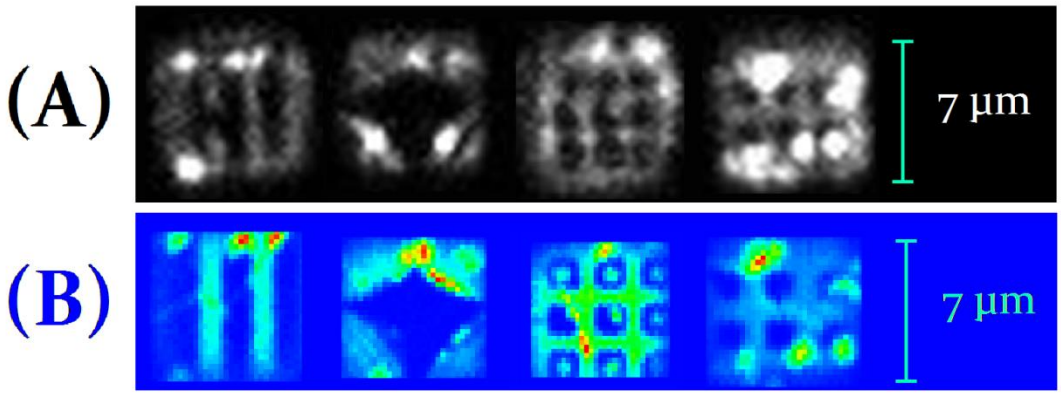

FIGURE 22. (A) wide-field FWM images of 7 x 7 μm^2 openings with oxidation patterns. (B) same openings imaged with scanning FWM.

each opening, without any observable features.

When compared to the images produced using raster-scanning FWM images (FIGURE 22), with patterning setup, the resolution and the contrast are slightly lower in wide-field FWM images, but while each raster-scanning image in FIGURE 21b was collected for minutes, the wide-field image of the whole area was recorded in 10 s.

The FWM wide-field imaging is indeed a convenient imaging method for characterizing graphene. It out-matches Raman and raster-scanning FWM microscopy in speed and provides proper information about the number of layers and morphology of graphene. With higher laser power, larger irradiation area, increased repetition rate, and proper optics the method could prove useful for large area characterization up to mm^2 scale.

3.3.2 FWM imaging graphene during photo-oxidation

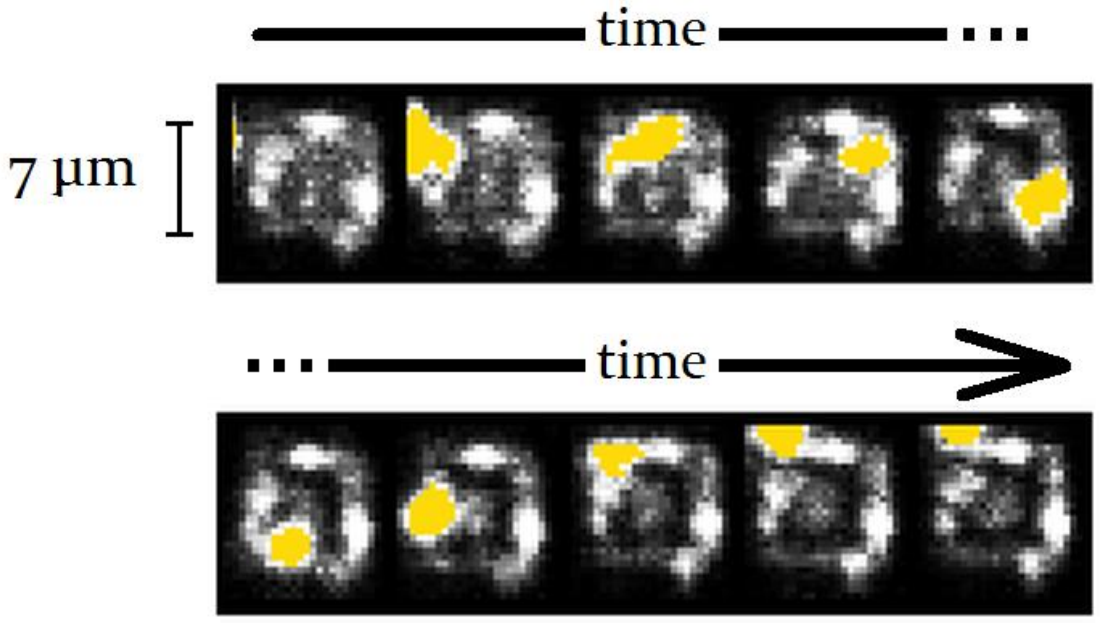

FIGURE 23. A cartoon of real time following of two-photon oxidation with wide-field FWM imaging. The yellow spot is the patternign beam and the greyish area is free-standing single layer graphene on 7x7 μm^2 opening. It is clear, that as the beam passes through the sample a the signal arising from square-shaped area diminishes to zero-level, leaving the center intact.

The excellent results in wide-field FMW microscopy motivated us to apply FWM imaging in observation of the oxidation process in real time. The patterning beam (590 nm) was brought in from behind and was filtered out using a dichroic mirror (FIGURE 13). Now, the FWM signal forming the image and additional patterning beam were visible on the detector simultaneously.

The patterning beam was moved on the sample manually and a video of the process was recorded. A square structure was patterned on graphene on an opening. A few-frame cartoon of the process is presented in FIGURE 23. The

intensity of the patterning beam could not be accurately measured but was estimated at $7.7 \cdot 10^{11} W/cm^2$, knowing the maximum intensity ($1.1 \cdot 10^{12} W/cm^2$) at an ND filter, located before on the beam was focused on the sample. This intensity fits the oxidation range discussed in Paper I, pointing towards oxidation instead of ablation.

This was the first time FWM imaging has been applied to real-time detection of chemical reaction induced with pulsed excitation. Graphene is an ideal sample for such study due to its high nonlinear optical response.

3.3.3 TR-CARS and G-mode dephasing dynamics

While Raman spectroscopy provides information about the steady state vibrational frequencies, band widths and intensities, all related to the structure of the material, time-resolved CARS can be utilized to characterize the coherent dynamics of the Raman active modes. The dynamics of graphene was measured with three-color TR-CARS spectroscopy. The used experimental arrangement allowed separation of various nonlinear processes, unambiguously, by spatially separating the generated CARS signals using non-collinear excitation geometry. The broader idea behind the time-resolved measurement is to eventually make the coherent dynamics measurement with wide-field imaging. Indeed, the same setup was utilized for both experiments, with just an alteration of the detection site.

The dynamics were measured from single layer graphene on Si/SiO_2. The sample was then tilted with respect to the normal of the excitation beams and detected from a reflected angle as described in FIGURE 14b.

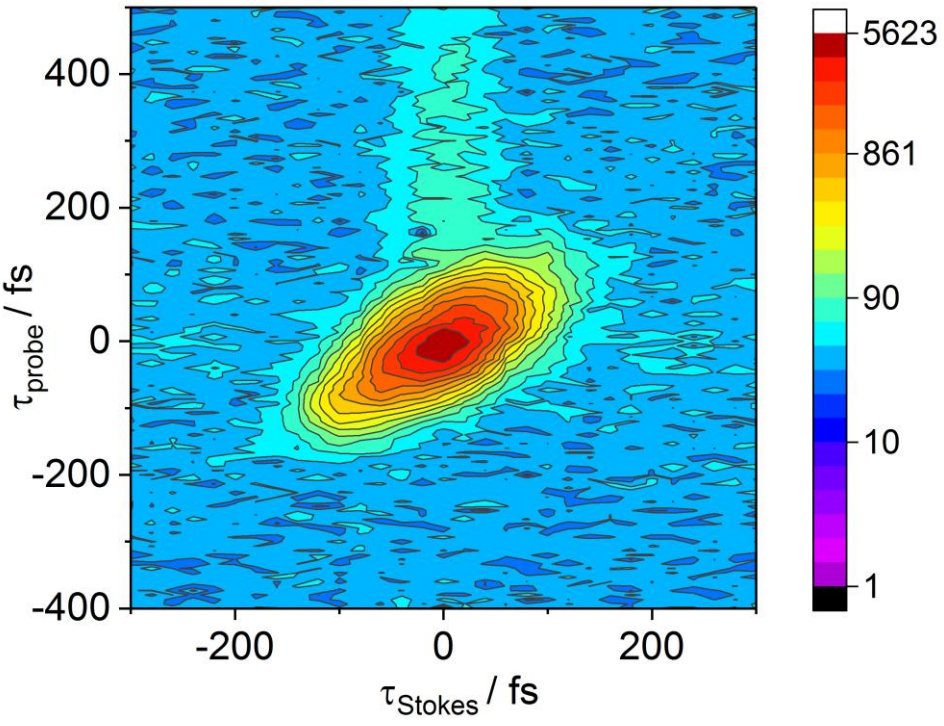

FIGURE 24. Intensity of CARS singnal ω_4 with respect to probe (vertical axis) and Stokes (horizontal axis). The values on the color bar represent signal intensity as photon counts.

When BOXCARS geometry was utilized for excitation, the generated CARS signals on the detector showed in total four different time-resolved signals, each corresponding to different non-linear processes originating from specific pulse sequences. The CARS signal ω_4 with wavelength 535 nm matching the conventional ordering of the pump (ω_1), Stokes (ω_2), and probe (ω_3) beam interactions $\omega_4(\omega_1, -\omega_2, \omega_3)$ and direction governed by the corresponding wave-vectors $\boldsymbol{k_4}(\boldsymbol{k_1}, -\boldsymbol{k_2}, \boldsymbol{k_3})$ was detected. The Stokes shift of ω_4 was assigned to overlap with the G-band of graphene. The CARS intensity profile of ω_4 is shown in FIGURE 24, where a long-lived decay with a lifetime ($T_2/2$) of 325 fs was present, primarily dependent on the delay between interactions of first and last beams.

The long-lived signal was designated as dephasing of the G-mode, which is in same order of magnitude with the G-band dephasing lifetime also found in earlier non-linear experiments.[131, 132] The G-band measured from the sample (FIGURE 25) is deconvoluted with instrumental function. This results in Lorentzian shape G-band with width of ~9 cm^{-1}, corresponding to $T_2/2$ = 590 fs.

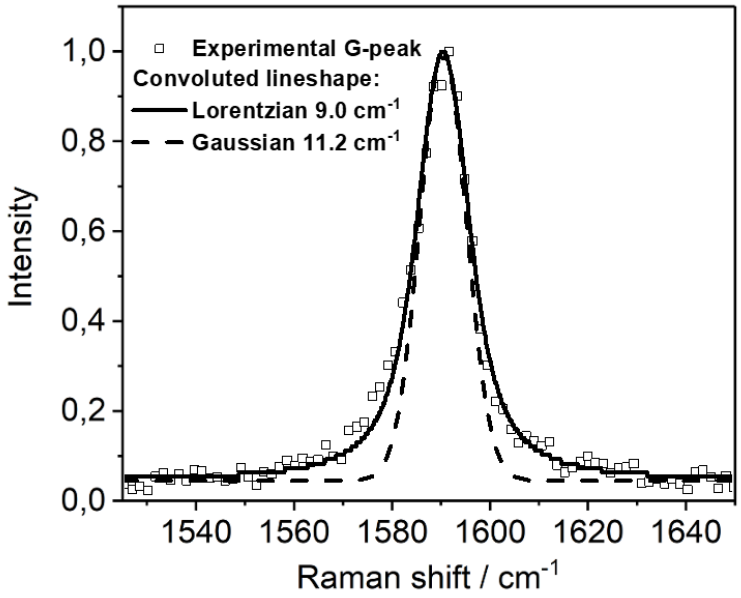

FIGURE 25. Raman G-band of the sample utilized in dynamics measurements. Results of G-band fitting. Lorentzian lineshape (FWHM 9.0 cm^{-1}) convoluted with Gaussian IRF (FWHM 7 cm^{-1}) solid line and convoluted Gaussian lineshape (FWHM 11.2 cm^{-1}) dashed line.

The accelerated dephasing time, observed in TR-CARS experiment, is caused by spectral diffusion, meaning dynamic electron-phonon decoupling, and thus the phonon frequency is affected by the electron population. Relating to FIGURE 11, when graphene is excited with pulsed laser, electron density is shifted from valence band to conduction band. The electronic temperature can be ~5000 K. Before the electron population relaxes back to valence band, it thermalizes with optical phonons. As the optical phonons are in quasi-equilibrium with the electrons they also experience a substantial temperature increase, and at ~1.0 ps the

temperature of these phonons along with the excitation may shift from ~300 to 2500 K. G-band position is known to disperse with changing temperature.[133] Also, the phonon frequency can be upshifted with electrostatic doping. As the phonons are coupled with electrons, the phonon frequency should alter with dynamic change of electron population in conduction band, that is, photoexcitation. While the electron population relaxes back to valence band, the phonon frequency downshifts to its initial value. The dynamic electron-phonon decoupling has been shown before for graphite.[132]
TR-CARS, done in reflection geometry for suspended samples, is applicable to measuring phonon dynamics in graphene. This combined with FWM wide-field microscopy should prove a powerful characterization method for imaging dynamics of graphene. With a single measurement, it reveals the spatial dynamics of different non-linear processes.

3.4 Possible new applications

In this section possible new applications that the results presented in this thesis could help uncover, are introduced. The size matters in technology, as the computational power of processors in smartphones, tablets, laptops etc. is directly dependent on the linewidth of transistors. Also, carbon is more abundant than silicon. It exists in all biological structures and it is preferable to remove carbon from the atmosphere in the form of CO_2 and CH_4, which contribute largely to global warming.

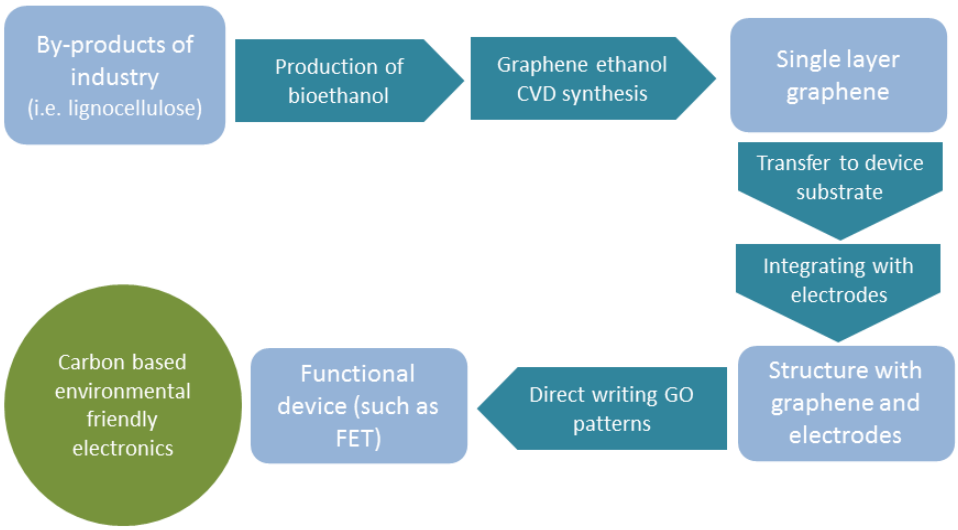

FIGURE 24. Schematic representation of the proposition of a production chain for carbon-based environmental friendly electronics.

3.4.1 Carbon based - environmental friendly electronics

The production chain starts with graphene synthesis with CVD, where bio-ethanol is utilized as a carbon source.[134] The graphene is then transferred to a substrate, suitable for the particular application, and patterned with the direct writing two-photon photo-oxidation using ultrafast pulsed lasers. The ethanol could be produced using side-products, generated by agricultural and pulp-and-paper industry, such as lignocellulose, which is produced nevertheless, and is currently mainly utilized for energy production or generation of bioethanol, which is further combusted, thus releasing CO_2 emissions into the atmosphere.[135]

All the steps in the production chain exist and are shown to work individually (FIGURE 26). Still, the process has several issues related to up-scaling the production chain and overcoming current competitive silicon technology. The laser patterning has been demonstrated to be applicable to fabrication of graphene-based devices with proof-of-concept field-effect transistor (FET) device, still a lot of research needs to be done involving how the experimental parameters, such as temporal pulse width, wavelength, pulse energy and irradiation time affect the chemical structure of the product, although some of these aspects have already been tested, such as the FET in Paper I.

The mass production of electronic devices or components by such a method could be sped-up. For this, a spatial light modulator (SLM) could be useful. Spatial light modulator is an electronic optical modulator, which is utilized for modulation of a beam into a programmed spatial pattern, by modulating amplitude, phase, or polarization of the beam. The SLM modifies the spot shape into a chosen image and can be utilized as an active mask. Optical modulators have been utilized with pulsed lasers before for patterning on materials by ablating.[136] For photo-oxidation, SLM could be utilized by using higher laser power, for example by applying directly the NOPA output, with a high repetition rate laser.

The linewidth for silicon-based transistors will be 10 nm in the next node of transistor technology, which is achieved by a technique involving extreme ultraviolet (~10 – 120 nm) lithography.[137] Wavelengths utilized in two-photon process are in visible range, and the pattern width is currently ~300 nm. By utilizing high numerical aperture (N.A.) objective perhaps linewidth ~150 nm could be achieved. Additionally, near-field methods (i.e., with scanning tunneling microscope tip), potentially ~10 nm linewidth could be reached.

3.4.2 Real-time following of Graphene growth

Another development presented in this thesis is wide-field FWM microscopy, which is a fast imaging method for graphene. The method could be used for monitoring growth of graphene in-situ. Ideally, the method would prove to be useful real-time quality control method as the graphene growth on the substrate, but also help uncover or further affirm the alleged mechanism of the

graphene growth on a surface. FWM wide-field imaging could be utilized for sub-micrometer patterns.

3.4.3 Humidity sensor

An ultrafast humidity sensor based on GO was tailored by Nokia in 2013.[138] The sensor is only 15 nm thick and approximately 10 mm in lateral dimensions. The two-photon oxidation patterning method could be utilized to fabricate a sensor chip with identical patterns that has 100 µm-size in lateral dimensions. Ten thousand sensors like this would fill the same area as the GO-based sensor presented by the Nokia research team. The function of the sensor is based on change on the impedance when GO interacts with the water molecules.[138] They reported response and recovery times of ~30 ms. As the size of a water molecule against the surface area of the detecting GO stripe would be higher for smaller stripes, the humidity sensors fabricated using the photo-oxidation patterning method would possess superior sensitivity to impedance changes and even faster response times. Also, significantly lower operational power consumption could be expected.[139]

GO–graphene combination is a good starting point for a moisture sensor, as graphene is hydrophobic and GO is hydrophilic. Also, the other molecules in air do not affect the GO in a way similar to water, making the sensor selective for H_2O. This type of sensor could be used in quality control of structures which should avoid contact with moisture. The measurements could possibly be conducted averaging results from several sensors locally, in order to improve the validity of the measurement. Although the device has not been demonstrated yet, it should be done in the near future to push the change in technology toward graphene based electronics.

3.4.4 Observing electron / phonon movement on graphene

The time-resolved CARS measurement of graphene G-band, achieved using BOXCARS geometry could be combined with the real-time wide-field imaging. By this approach, spatial distribution of s CARS signal could be observed in graphene. Due to long coherence length of graphene, the carrier movement resulted from pulsed excitation, could be monitored. Then again, by using longer collection times the spatially resolved phonon dephasing on graphene surface could be imaged. Also, an interesting aspect would be to see how CARS signal, either the electronic part or the vibration dephasing, behaves in graphene-GO interfaces or graphene-metal interfaces.

4 SUMMARY AND CONCLUSIONS

Ultrafast light-matter interactions of graphene were investigated with femtosecond lasers. Irradiation of graphene with laser pulses in air led to photo-oxidation of graphene, resulting to opened band gap. This phenomenon was used for controlled patterning of graphene. The structure patterns produced with the oxidation method were investigated with Raman, AFM, μ-XPS and phenomenological simulations. It was revealed that the oxidation initiates from point-like sources, which evolve into islands with increasing irradiation doses, ultimately leading to coalescence of islands after they reach ~30-40 nm diameter. During the initial steps of oxidation them, with the help of moisture, adsorbed oxygen molecules attach to graphene forming hydroxyl and epoxide groups, causing change in proportions of sp^2 and sp^3 carbons. Subsequently, the oxygen content of the patterned areas increases. Rapid increase of degree of oxidation occurs with coalescence of oxidized islands. Ultimately, ~65 % of carbon atoms are involved in these chemical groups.

Also, nonlinear optical interactions were utilized to develop a characterization method for graphene, a wide-field FWM microscopy. Due to the strong third-order non-linear response of graphene the images from 50 x 50 um2 area with high contrast are obtained within seconds and the oxidized patterns are observed clearly. The potential of the method was demonstrated by observing real-time photo-oxidation of graphene, which shows a promise for utilization the method for investigation of other processes, such as graphene growth in a CVD chamber, in real-time.

Additionally, the dephasing dynamics of phonons in graphene were investigated with CARS measurements for the first time. Long-lived coherent signal was observed and it was assigned to the coherent excitation of the G-mode. The dephasing time of the G-mode was 325 fs, which is shortened by redistribution of photo-induced carrier density distribution, which affects dynamically the G-mode frequency due to non-adiabatic decoupling between phonons and electrons.

REFERENCES

1. J.C. Meyer, A.K. Geim, M.I. Katsnelson, K.S. Novoselov, T.J. Booth and S. Roth, The structure of suspended graphene sheets, *Nature,* **2007**, *446*(7131), 60-63.

2. E. Stolyarova, K.T. Rim, S. Ryu, J. Maultzsch, P. Kim, L.E. Brus, T.F. Heinz, M.S. Hybertsen and G.W. Flynn, High-resolution scanning tunneling microscopy imaging of mesoscopic graphene sheets on an insulating surface, *PNAS,* **2007**, *104*(22), 9209-9212.

3. J. Chen, C. Jang, S. Xiao, M. Ishigami and M.S. Fuhrer, Intrinsic and extrinsic performance limits of graphene devices on SiO2, *Nat Nano,* **2008**, *3*(4), 206-209.

4. J. Chen, C. Jang, S. Adam, M.S. Fuhrer, E.D. Williams and M. Ishigami, Charged-impurity scattering in graphene, *Nat Phys,* **2008**, *4*(5), 377-381.

5. K.S. Novoselov, A.K. Geim, S.V. Morozov, D. Jiang, M.I. Katsnelson, I.V. Grigorieva, S.V. Dubonos and A.A. Firsov, Two-dimensional gas of massless dirac fermions in graphene, *Nature,* **2005**, *438*(7065), 197-200.

6. A.A. Balandin, S. Ghosh, W. Bao, I. Calizo, D. Teweldebrhan, F. Miao and C.N. Lau, Superior thermal conductivity of single-layer graphene, *Nano Lett.,* **2008**, *8*(3), 902-907.

7. C. Lee, X. Wei, J.W. Kysar and J. Hone, Measurement of the elastic properties and intrinsic strength of monolayer graphene, *Science,* **2008**, *321*(5887), 385-388.

8. E. Hendry, P.J. Hale, J. Moger, A.K. Savchenko and S.A. Mikhailov, Coherent nonlinear optical response of graphene, *Phys. Rev. Lett.,* **2010**, *105*(9), 097401.

9. Y. Lin, A. Valdes-Garcia, S. Han, D.B. Farmer, I. Meric, Y. Sun, Y. Wu, C. Dimitrakopoulos, A. Grill, P. Avouris and K.A. Jenkins, Wafer-scale graphene integrated circuit, *Science,* **2011**, *332*(6035), 1294-1297.

10. A. Nathan, A. Ahnood, M.T. Cole, S. Lee, Y. Suzuki, P. Hiralal, F. Bonaccorso, T. Hasan, L. Garcia-Gancedo, A. Dyadyusha, S. Haque, P. Andrew, S. Hofmann, J. Moultrie, D. Chu, A.J. Flewitt, A.C. Ferrari, M.J. Kelly, J. Robertson, G.A.J. Amaratunga and W.I. Milne, Flexible electronics: The next ubiquitous platform, *Proceedings of the IEEE,* **2012**, *100*(Special Centennial Issue), 1486-1517.

11. F. Torrisi, T. Hasan, W. Wu, Z. Sun, A. Lombardo, T.S. Kulmala, G. Hsieh, S. Jung, F. Bonaccorso, P.J. Paul, D. Chu and A.C. Ferrari, Inkjet-printed graphene electronics, *ACS Nano,* **2012**, *6*(4), 2992-3006.

12. M. Bernardi, M. Palummo and J.C. Grossman, Extraordinary sunlight absorption and one nanometer thick photovoltaics using two-dimensional monolayer materials, *Nano Lett.,* **2013**, *13*(8), 3664-3670.

13. X. Li, M. Rui, J. Song, Z. Shen and H. Zeng, Carbon and graphene quantum dots for optoelectronic and energy devices: A review, *Adv. Funct. Mater.,* **2015**, *25*(31), 4929-4947.

14. K.S. Kim, Y. Zhao, H. Jang, S.Y. Lee, J.M. Kim, K.S. Kim, J. Ahn, P. Kim, J. Choi and B.H. Hong, Large-scale pattern growth of graphene films for stretchable transparent electrodes, *Nature,* **2009**, *457*(7230), 706-710.

15. A. Pospischil, M. Humer, M.M. Furchi, D. Bachmann, R. Guider, T. Fromherz and T. Mueller, CMOS-compatible graphene photodetector covering all optical communication bands, *Nat Photon,* **2013**, *7*(11), 892-896.

16. L. Guo, R. Shao, Y. Zhang, H. Jiang, X. Li, S. Xie, B. Xu, Q. Chen, J. Song and H. Sun, Bandgap tailoring and synchronous microdevices patterning of graphene oxides, *J. Phys. Chem. C,* **2012**, *116*(5), 3594-3599.

17. K.S. Novoselov, A.K. Geim, S.V. Morozov, D. Jiang, Y. Zhang, S.V. Dubonos, I.V. Grigorieva and A.A. Firsov, Electric field effect in atomically thin carbon films, *Science,* **2004**, *306*(5696), 666-669.

18. A.C. Ferrari, F. Bonaccorso, V. Fal'ko, K.S. Novoselov, S. Roche, P. Bøggild, S. Borini, F.H.L. Koppens, V. Palermo, N. Pugno, J.A. Garrido, R. Sordan, A. Bianco, L. Ballerini, M. Prato, E. Lidorikis, J. Kivioja, C. Marinelli, T. Ryhänen, A. Morpurgo, J.N. Coleman, V. Nicolosi, L. Colombo, A. Fert, M. Garcia-Hernandez, A. Bachtold, G.F. Schneider, F. Guinea, C. Dekker, M. Barbone, Z. Sun, C. Galiotis, A.N. Grigorenko, G. Konstantatos, A. Kis, M. Katsnelson, L. Vandersypen, A. Loiseau, V. Morandi, D. Neumaier, E. Treossi, V. Pellegrini, M. Polini, A. Tredicucci, G.M. Williams, B.H. Hong, J. Ahn, J.M. Kim, H. Zirath, B.J.v. Wees, H.v.d. Zant, L. Occhipinti, A.D. Matteo, I.A. Kinloch, T. Seyller, E. Quesnel, X. Feng, K. Teo, N. Rupesinghe, P. Hakonen, S.R.T. Neil, Q. Tannock, T. Löfwander and J. Kinaret, Science and technology roadmap for graphene, related two-dimensional crystals, and hybrid systems, *Nanoscale,* **2015**, *7*(11), 4598-4810.

19. Y.R. Jang, K.Y. Kim and K.H. Yoo, Accurate measurement of thickness of large-area graphene layers by neutron reflectometry, *J Mater Sci,* **2016**, *51*(22), 10059-10065.

20. C. Housecroft and E. Constable, *Chemistry*, 3rd painos, Pearson Education Limited, 2006.

21. N.M.R. Peres, Colloquium: The transport properties of graphene: An introduction, *Rev. Mod. Phys.,* **2010**, *82*(3), 2673-2700.

22. P.A.M. Dirac, *The principles of quantum mechanics*, 4.ed.rev., repr. painos, Clarendon Pr, Oxford, 1981.

23. K.S. Novoselov, A.K. Geim, S.V. Morozov, D. Jiang, M.I. Katsnelson, I.V. Grigorieva, S.V. Dubonos and A.A. Firsov, Two-dimensional gas of massless dirac fermions in graphene, *Nature,* **2005**, *438*(7065), 197-200.

24. X. Du, I. Skachko, A. Barker and E.Y. Andrei, Approaching ballistic transport in suspended graphene, *Nat Nano,* **2008**, *3*(8), 491-495.

25. S. Ji, J.B. Hannon, R.M. Tromp, V. Perebeinos, J. Tersoff and F.M. Ross, Atomic-scale transport in epitaxial graphene, *Nat Mater,* **2012**, *11*(2), 114-119.

26. Y. Tan, Y. Zhang, K. Bolotin, Y. Zhao, S. Adam, E.H. Hwang, S. Das Sarma, H.L. Stormer and P. Kim, Measurement of scattering rate and minimum conductivity in graphene, *Phys. Rev. Lett.,* **2007**, *99*(24), 246803.

27. R.R. Nair, P. Blake, A.N. Grigorenko, K.S. Novoselov, T.J. Booth, T. Stauber, N.M.R. Peres and A.K. Geim, Fine structure constant defines visual transparency of graphene, *Science,* **2008**, *320*(5881), 1308.

28. C. Soldano, A. Mahmood and E. Dujardin, Production, properties and potential of graphene, *Carbon,* **2010**, *48*(8), 2127-2150.

29. J.H. Seol, I. Jo, A.L. Moore, L. Lindsay, Z.H. Aitken, M.T. Pettes, X. Li, Z. Yao, R. Huang, D. Broido, N. Mingo, R.S. Ruoff and L. Shi, Two-dimensional phonon transport in supported graphene, *Science,* **2010**, *328*(5975), 213-216.

30. Z. Chen, W. Jang, W. Bao, C. N. Lau and C. Dames. Thermal contact resistance between graphene and silicon dioxide, *Appl. Phys. Lett.,* **2009**, *95*(16), 161910.

31. S. Pisana, M. Lazzeri, C. Casiraghi, K.S. Novoselov, A.K. Geim, A.C. Ferrari and F. Mauri, Breakdown of the adiabatic Born–Oppenheimer approximation in graphene, *Nat Mater,* **2007**, *6*(3), 198-201.

32. Y. Zhang, Y. Tan, H.L. Stormer and P. Kim, Experimental observation of the quantum hall effect and berry's phase in graphene, *Nature,* **2005**, *438*(7065), 201-204.

33. M.I. Katsnelson, K.S. Novoselov and A.K. Geim, Chiral tunnelling and the klein paradox in graphene, *Nature Physics,* **2006**, *2*(9), 620-625.

34. A.F. Young and P. Kim, Quantum interference and klein tunnelling in graphene heterojunctions, *Nature Physics,* **2009**, *5*(3), 222-226.

35. A. Kumar and C. Zhou, The race to replace tin-doped indium oxide: Which material will win? *ACS Nano,* **2010**, *4*(1), 11-14.

36. Z. Chen, B. Cotterell, W. Wang, E. Guenther and S. Chua, A mechanical assessment of flexible optoelectronic devices, *Thin Solid Films,* **2001**, *394*(1–2), 201-205.

37. S.P. Koenig, N.G. Boddeti, M.L. Dunn and J.S. Bunch, Ultrastrong adhesion of graphene membranes, *Nat Nano,* **2011**, *6*(9), 543-546.

38. F. Torrisi, T. Hasan, W. Wu, Z. Sun, A. Lombardo, T.S. Kulmala, G. Hsieh, S. Jung, F. Bonaccorso, P.J. Paul, D. Chu and A.C. Ferrari, Inkjet-printed graphene electronics, *ACS Nano,* **2012**, *6*(4), 2992-3006.

39. H. Sundmaeker, P. Guillemin and P. Friess and S. Woelffle, Vision and Challenges for Realising the Internet of Things, **2010**, 229 pages.

40. R. Cheng, J. Bai, L. Liao, H. Zhou, Y. Chen, L. Liu, Y. Lin, S. Jiang, Y. Huang and X. Duan. High-frequency self-aligned graphene transistors with transferred gate stacks, *Proceedings of the National Academy of Sciences of the United States of America,* **2012**, *109*(29), 11588-11592.

41. E.U. Stützel, M. Burghard, K. Kern, F. Traversi, F. Nichele and R. Sordan, A graphene nanoribbon memory cell, *Small,* **2010**, *6*(24), 2822-2825.

42. F. Schwierz, Graphene transistors, *Nature Nanotechnology,* **2010**, *5*(7), 487-496.

43. E. Guerriero, L. Polloni, M. Bianchi, A. Behnam, E. Carrion, L.G. Rizzi, E. Pop and R. Sordan, Gigahertz integrated graphene ring oscillators, *ACS nano,* **2013**, *7*(6), 5588.

44. D.C. Elias, R.R. Nair, T.M.G. Mohiuddin, S.V. Morozov, P. Blake, M.P. Halsall, A.C. Ferrari, D.W. Boukhvalov, M.I. Katsnelson, A.K. Geim and K.S. Novoselov, Control of graphene's properties by reversible hydrogenation: Evidence for graphane, *Science,* **2009**, *323*(5914), 610-613.

45. R.R. Nair, W. Ren, R. Jalil, I. Riaz, V.G. Kravets, L. Britnell, P. Blake, F. Schedin, A.S. Mayorov, S. Yuan, M.I. Katsnelson, H. Cheng, W. Strupinski, L.G. Bulusheva, A.V. Okotrub, I.V. Grigorieva, A.N. Grigorenko, K.S. Novoselov and A.K. Geim, Fluorographene: A two-dimensional counterpart of teflon, *Small,* **2010**, *6*(24), 2877-2884.

46. A. Urich, K. Unterrainer and T. Mueller, Intrinsic response time of graphene photodetectors, *Nano letters,* **2011**, *11*(7), 2804.

47. Z. Sun, T. Hasan, F. Torrisi, D. Popa, G. Privitera, F. Wang, F. Bonaccorso, D.M. Basko and A.C. Ferrari, Graphene mode-locked ultrafast laser, *ACS nano,* **2010**, *4*(2), 803.

48. L. Vicarelli, M.S. Vitiello, D. Coquillat, A. Lombardo, A.C. Ferrari, W. Knap, M. Polini, V. Pellegrini and A. Tredicucci, Graphene field-effect transistors as room-temperature terahertz detectors, *Nature materials,* **2012**, *11*(10), 865.

49. G. Konstantatos, M. Badioli, L. Gaudreau, J. Osmond, M. Bernechea, F. P. Garcia De Arquer, F. Gatti and F. H. L. Koppens, Hybrid graphene-quantum dot phototransistors with ultrahigh gain, *Nature Nanotechnology,* **2012**, *7*(6), 363.

50. H. Yan, X. Li, B. Chandra, G. Tulevski, Y. Wu, M. Freitag, W. Zhu, P. Avouris and F. Xia, Tunable infrared plasmonic devices using graphene/insulator stacks, *Nat Nanotechnol,* **2012**, *7*(5), 330-334.

51. L. Ju, B. Geng, J. Horng, C. Girit, M. Martin, Z. Hao, H. A. Bechtel, X. Liang, A. Zettl, Y. R. Shen and F. Wang, Graphene plasmonics for tunable terahertz metamaterials, *Nature Nanotechnology,* **2011**, *6*(10), 630-634.

52. J. Yan, M.-H. Kim, J. A. Elle, A. B. Sushkov, G. S. Jenkins, H. M. Milchberg, M. S. Fuhrer and H. D. Drew, Dual-gated bilayer graphene hot-electron bolometer, *Nature Nanotechnology,* **2012**, *7*(7), 472.

53. M. Mittendorff, S. Winnerl, J. Kamann, J. Eroms, D. Weiss, H. Schneider and M. Helm, Ultrafast graphene-based broadband THz detector, *Applied Physics Letters,* **2013**, *103*(2), 21113.

54. V. Ryzhii, V. Aleshkin, M. Ryzhii, T. Otsuji, A. Satou and A. Dubinov, Feasibility of terahertz lasing in optically pumped epitaxial multiple graphene layer structures, *Journal of Applied Physics,* **2009**, *106*(8), 6.

55. X. Yang, G. Liu, A.A. Balandin and K. Mohanram, Triple-mode single-transistor graphene amplifier and its applications, *ACS Nano,* **2010**, *4*(10), 5532-5538.

56. C. Feng, Y. Wang, J. Liu, Y.H. Tsang, Y. Song and Z. Yu, 3 W high-power laser passively mode-locked by graphene oxide saturable absorber, *Optics Communications,* **2013**, *298–299*, 168-170.

57. C.-. Wong, M. Annamalai, Z.-. Wang and M. Palaniapan, Characterization of nanomechanical graphene drum structures, *J. Micromech. Microeng.,* **2010**, *20*(11), 115029.

58. Y. Liu, X. Dong and P. Chen, Biological and chemical sensors based on graphene materials, *Chemical Society reviews,* **2012**, *41*(6), 2283-237.

59. F. Yavari and N. Koratkar, Graphene-based chemical sensors, *The journal of physical chemistry letters,* **2012**, *3*(13), 1746.

60. S. Bae, Y. Lee, B.K. Sharma, H. Lee, J. Kim and J. Ahn, Graphene-based transparent strain sensor, *Carbon,* **2013**, *51*, 236-242.

61. A.H. Castro Neto and F. Guinea, Impurity-induced spin-orbit coupling in graphene, *Phys. Rev. Lett.,* **2009**, *103*(2), 026804.

62. J. Balakrishnan, G. K. W. Koon, M. Jaiswal, A. H. C. Neto and B. Özyilmaz, Colossal enhancement of spin-orbit coupling in weakly hydrogenated graphene, *Nature Physics,* **2013**, *9*(5), 284.

63. B. Trauzettel, D. V. Bulaev, D. Loss and G. Bukard, Spin qubits in graphene quantum dots, *Nat Phys,* **2007**, *3*, 192-196.

64. D. Loss and D.P. DiVincenzo, Quantum computation with quantum dots, *Physical Review A,* **1998**, *57*(1), 120-126.

65. D. Bitounis, H. Ali-Boucetta, B. Hee Hong, D.-H. Min and K. Kostarelos, Prospects and challenges of graphene in biomedical applications, Advanced materials (Deerfield Beach, Fla.), 25, 2013, 2258-2268.

66. J. Hassoun, F. Bonaccorso, M. Agostini, M. Angelucci, M.G. Betti, R. Cingolani, M. Gemmi, C. Mariani, S. Panero, V. Pellegrini and B. Scrosati, An advanced lithium-ion battery based on a graphene anode and a lithium iron phosphate cathode, *Nano letters,* **2014**, *14*(8), 4901.

67. X. Miao, S. Tongay, M.K. Petterson, K. Berke, A.G. Rinzler, B.R. Appleton and A.F. Hebard, High efficiency graphene solar cells by chemical doping, *Nano letters,* **2012**, *12*(6), 2745.

68. G. Nandamuri, S. Roumimov and R. Solanki, Chemical vapor deposition of graphene films, *Nanotechnology,* **2010**, *21*(14), 145604.

69. A. Reina, S. Thiele, X. Jia, S. Bhaviripudi, M.S. Dresselhaus, J.A. Schaefer and J. Kong, Growth of large-area single- and bi-layer graphene by controlled carbon precipitation on polycrystalline ni surfaces, *Nano Res.,* **2009**, *2*(6), 509-516.

70. A. Guermoune, T. Chari, F. Popescu, S.S. Sabri, J. Guillemette, H.S. Skulason, T. Szkopek and M. Siaj, Chemical vapor deposition synthesis of graphene on copper with methanol, ethanol, and propanol precursors, *Carbon,* **2011**, *49*(13), 4204-4210.

71. P.W. Sutter, J. Flege and E.A. Sutter, Epitaxial graphene on ruthenium, *Nature Materials,* **2008**, *7*(5), 406-411.

72. O. Nakagoe, N. Takagi and Y. Matsumoto, Thermal decomposition of acetylene on Pt(1 1 1) studied by scanning tunneling microscopy, *Surface Science,* **2002**, *514*(1–3), 414-419.

73. S.Y. Lee, H. Jang, K.S. Kim, J. Ahn, P. Kim, J.M. Kim, B.H. Hong, J. Choi, K.S. Kim and Y. Zhao, Large-scale pattern growth of graphene films for stretchable transparent electrodes, *Nature,* **2009**, *457*(7230), 706-710.

74. W. A. de Heer, C. Berger, M. Ruan, M. Sprinkle, X. Li, Y. Hu, B. Zhang, J. Hankinson and E. Conrad, Large area and structured epitaxial graphene produced by confinement controlled sublimation of silicon carbide, *Proceedings of the National Academy of Sciences of the United States of America,* **2011**, *108*(41), 16900-16905.

75. A.G. Cano-Márquez, F.J. Rodríguez-Macías, J. Campos-Delgado, C.G. Espinosa-González, F. Tristán-López, D. Ramírez-González, D.A. Cullen, D.J. Smith, M. Terrones and Y.I. Vega-Cantú, Ex-MWNTs: Graphene sheets and ribbons produced by lithium intercalation and exfoliation of carbon nanotubes, *Nano Lett.,* **2009**, *9*(4), 1527-1533.

76. A.N. Obraztsov, A.A. Zolotukhin, A.O. Ustinov, A.P. Volkov, Y. Svirko and K. Jefimovs, DC discharge plasma studies for nanostructured carbon CVD, *Diamond and Related Materials,* **2003**, *12*(3–7), 917-920.

77. L. Song, L. Ci, W. Gao and P.M. Ajayan, Transfer printing of graphene using gold film, *ACS nano,* **2009**, *3*(6), 1353.

78. J. Shang, L. Ma, J. Li, W. Ai, T. Yu and G.G. Gurzadyan, The origin of fluorescence from graphene oxide, *Scientific reports,* **2012**, *2*, 792.

79. O.C. Compton and S.T. Nguyen, Graphene oxide, highly reduced graphene oxide, and graphene: Versatile building blocks for carbon-based materials, *Small (Weinheim an der Bergstrasse, Germany),* **2010**, *6*(6), 711-723.

80. E.F. Sheka and N.A. Popova, *PCCP*, The Royal Society of Chemistry, 2013.

81. Brodie and B. C., On the atomic weight of graphite, *Phil. Trans. R. Soc. Lond,* **1859**, *149*, 249-259.

82. M. Hirata, T. Gotou, S. Horiuchi, M. Fujiwara and M. Ohba, Thin-film particles of graphite oxide 1:High-yield synthesis and flexibility of the particles, *Carbon,* **2004**, *42*(14), 2929-2937.

83. W. Cai, R. D. Piner, F. J. Stadermann, S. Park, M. A. Shaibat, Y. Ishii, D. Yang, A. Velamakanni, S. J. An, M. Stoller, J. An, D. Chen and R. S. Ruoff, Synthesis and solid-state NMR structural characterization of 13C-labeled graphite oxide, *Science,* **2008**, *321*(5897), 1815-1817.

84. K. Krishnamoorthy, M. Veerapandian, K. Yun and S.-. Kim, The chemical and structural analysis of graphene oxide with different degrees of oxidation, *Carbon,* **2013**, *53*, 38-49.

85. S. Zhao, S.P. Surwade, Z. Li and H. Liu, Photochemical oxidation of CVD-grown single layer graphene, *Nanotechnology,* **2012**, *23*(35), 355703.

86. M. Yamamoto, T.L. Einstein, M.S. Fuhrer and W.G. Cullen, Charge inhomogeneity determines oxidative reactivity of graphene on substrates, *ACS nano,* **2012**, *6*(9), 8335.

87. S. Pei and H. Cheng, The reduction of graphene oxide, *Carbon,* **2012**, *50*(9), 3210-3228.

88. D.A. Long, *The Raman Effect*, Wiley, Chichester, **2002**.

89. P.W. Atkins and R. Friedman, *Molecular Quantum Mechanics*, 4. ed., reprinted (with corr.) painos, Oxford Univ. Press, Oxford, **2007**.

90. A. C. Ferrari and D. M. Basko, Raman spectroscopy as a versatile tool for studying the properties of graphene, *Nature Nanotechnology,* **2013**, *8*(4), 235.

91. A.C. Ferrari, Raman spectroscopy of graphene and graphite: Disorder, electron–phonon coupling, doping and nonadiabatic effects, *Solid State Communications,* **2007**, *143*(1–2), 47-57.

92. J. Kim, A.R.T. Nugraha, L.G. Booshehri, E.H. Hároz, K. Sato, G.D. Sanders, K. Yee, Y.-. Lim, C.J. Stanton, R. Saito and J. Kono, Coherent phonons in carbon nanotubes and graphene, *Chemical Physics,* **2013**, *413*, 55-80.

93. M.S. Dresselhaus, G. Dresselhaus and P.C. Eklund, Raman scattering in fullerenes, *J. Raman Spectrosc.,* **1996**, *27*(3-4), 351-371.

94. K. Kneipp, H. Kneipp, P. Corio, S.D.M. Brown, K. Shafer, J. Motz, L.T. Perelman, E.B. Hanlon, A. Marucci, G. Dresselhaus and M.S. Dresselhaus, Surface-enhanced and normal stokes and anti-stokes raman spectroscopy of single-walled carbon nanotubes, *Phys. Rev. Lett.,* **2000**, *84*(15), 3470-3473.

95. V. Mennella, G. Monaco, L. Colangeli and E. Bussoletti, Raman spectra of carbon-based materials excited at 1064 nm, *Carbon,* **1995**, *33*(2), 115-121.

96. A. Gupta, G. Chen, P. Joshi, S. Tadigadapa and P.C. Eklund, Raman scattering from high-frequency phonons in supported n-graphene layer films, *Nano letters,* **2006**, *6*(12), 2667.

97. Y. Wang, Z. Ni, T. Yu, Z. X. Shen, H. Wang, Y. Wu, W. Chen and A. T. S. Wee, Raman Studies of Monolayer Graphene: The Substrate Effect, *J. Phys. Chem. C*, **2008**, *112*, 10637-10640.

98. A. Das, B. Chakraborty and A.K. Sood, Raman spectroscopy of graphene on different substrates and influence of defects, *Bull Mater Sci,* **2008**, *31*(3), 579-584.

99. S. Berciaud, S. Ryu, L.E. Brus and T.F. Heinz, Probing the intrinsic properties of exfoliated graphene: Raman spectroscopy of free-standing monolayers, *Nano Lett.,* **2009**, *9*(1), 346-352.

100. I. Calizo, S. Ghosh, W. Bao, F. Miao, C. Ning Lau and A.A. Balandin, Raman nanometrology of graphene: Temperature and substrate effects, *Solid State Communications,* **2009**, *149*(27–28), 1132-1135.

101. C Bousige, F Balima, D Machon, G S Pinheiro, A Torres-Dias, J Nicolle, D Kalita, N Bendiab, L Marty, V Bouchiat, G Montagnac, A G Souza Filho, P Poncharal and A San-Miguel, Biaxial strain transfer in supported graphene, *Nano letters,* **2017**, *17*(1), 21-27.

102. M.M. Lucchese, F. Stavale, E.H.M. Ferreira, C. Vilani, M.V.O. Moutinho, R.B. Capaz, C.A. Achete and A. Jorio, Quantifying ion-induced defects and raman relaxation length in graphene, *Carbon,* **2010**, *48*(5), 1592-1597.

103. A. Eckmann, A. Felten, A. Mishchenko, L. Britnell, R. Krupke, K.S. Novoselov and C. Casiraghi, Probing the nature of defects in graphene by raman spectroscopy, *Nano letters,* **2012**, *12*(8), 3925.

104. S. Pisana, S.K. Saha, A.C. Ferrari, A.K. Sood, K.S. Novoselov, A.K. Geim, B. Chakraborty, U.V. Waghmare, A. Das, S. Piscanec and H.R. Krishnamurthy, Monitoring dopants by raman scattering in an electrochemically top-gated graphene transistor, *Nature Nanotechnology,* **2008**, *3*(4), 210-215.

105. F. Herziger, R. Mirzayev, E. Poliani and J. Maultzsch, In-situ raman study of laser-induced graphene oxidation, *Phys. Status Solidi B,* **2015**, *252*(11), 2451-2455.

106. A.H. Zewail, Femtochemistry: Atomic-scale dynamics of the chemical bond, *The Journal of Physical Chemistry A,* **2000**, *104*(24), 5660-5694.

107. D.J. Tannor, *Introduction to quantum mechanics : a time-dependent perspective*, University Science Books, Sausalito, Calif, **2007**.

108. R.L. Carman, R.Y. Chiao and P.L. Kelley, Observation of degenerate stimulated four-photon interaction and four-wave parametric amplification, *Physical Review Letters,* **1966**, *17*(26), 1281-1283.

109. P.D. Maker and R.W. Terhune, Study of optical effects due to an induced polarization third-order in the electric field strength, *Physical Review,* **1965**, *137*(3A), A818.

110. P. Myllyperkiö, O. Herranen, J. Rintala, H. Jiang, P.R. Mudimela, Z. Zhu, A.G. Nasibulin, A. Johansson, E.I. Kauppinen, M. Ahlskog and M. Pettersson, Femtosecond four-wave-mixing spectroscopy of suspended individual semiconducting single-walled carbon nanotubes, *ACS nano,* **2010**, *4*(11), 6780.

111. T. Sheps, J. Brocious, B. L. Corso, O. T. Gül, D. Whitmore, G. Durkaya, E. O. Potma, and P. G. Collins. Four-wave mixing microscopy with electronic contrast of individual carbon nanotubes. *Phys. Rev. B*, **2012**, *86*, 235412

112. J. Reintjes, M. D. Duncan and T. J. Manuccia, Picosecond coherent anti-stokes raman scattering (CARS) microscope, *Proc. SPIE,* **1982**, *322*, 87-93.

113. Y. Wang, X. Liu, A.R. Halpern, K. Cho, R.M. Corn and E.O. Potma, Wide-field, surface-sensitive four-wave mixing microscopy of nanostructures, *Appl. Opt., AO,* **2012**, *51*(16), 3305-3312.

114. A. Säynätjoki, L. Karvonen, J. Riikonen, W. Kim, S. Mehravar, R.A. Norwood, N. Peyghambarian, H. Lipsanen and K. Kieu, Rapid large-area multiphoton microscopy for characterization of graphene, *ACS nano,* **2013**, *7*(10), 8441.

115. D.W. Li, Y.S. Zhou, X. Huang, L. Jiang, J. Silvain and Y.F. Lu, In situ imaging and control of layer-by-layer femtosecond laser thinning of graphene, *Nanoscale,* **2015**, *7*(8), 3651-3659.

116. M. Spencer, M. Chandrashekhar, J. Dawlaty, S. Shivaraman and F. Rana, Measurement of ultrafast carrier dynamics in epitaxial graphene, *Applied Physics Letters,* **2008**, *92*(4), 3.

117. M. Breusing, S. Kuehn, T. Winzer, E. Malić, F. Milde, N. Severin, J.P. Rabe, C. Ropers, A. Knorr and T. Elsaesser, Ultrafast nonequilibrium carrier dynamics in a single graphene layer, *Physical Review B,* **2011**, *83*(15).

118. C. Bronner, D. Gerbert, A. Broska and P. Tegeder, Excitonic states in narrow armchair graphene nanoribbons on gold surfaces, *J. Phys. Chem. C,* **2016**, *120*(45), 26168-26172.

119. D. Giovanni, G. Yu, G. Xing, M.L. Leek and T.C. Sum, Measurement of sub-10 fs auger processes in monolayer graphene, *Optics express,* **2015**, *23*(16), 21107.

120. T J Constant, S M Hornett, D E Chang and E Hendry, All-optical generation of surface plasmons in graphene, *Nature Physics,* **2016**, *12*(2), 124.

121. P.A. George, J. Strait, J. Dawlaty, S. Shivaraman, M. Chandrashekhar, F. Rana and M.G. Spencer, Ultrafast optical-pump terahertz-probe spectroscopy of the carrier relaxation and recombination dynamics in epitaxial graphene, *Nano letters,* **2008**, *8*(12), 4248-4251.

122. T. Winzer and E. Malić, Impact of auger processes on carrier dynamics in graphene, *Phys. Rev. B,* **2012**, *85*(24), 241404.

123. K. Kaasbjerg, K.S. Thygesen and K.W. Jacobsen, Unraveling the acoustic electron-phonon interaction in graphene, *Phys. Rev. B,* **2012**, *85*(16), 165440.

124. World Health Organization, WHO-Europe report, **2003**, 92 pages.

125. I. Bobrinetskiy, A. Emelianov, A. Nasibulin, I. Komarov, N. Otero and P.M. Romero, Photophysical and photochemical effects in ultrafast laser patterning of CVD graphene, *J. Phys. D: Appl. Phys.,* **2016**, *49*(41), 41LT01.

126. S. Ryu, L. Liu, S. Berciaud, Y. Yu, H. Liu, P. Kim, G.W. Flynn and L.E. Brus, Atmospheric oxygen binding and hole doping in deformed graphene on a SiO_2 substrate, *Nano letters,* **2010**, *10*(12), 4944.

127. A. Eckmann, A. Felten, A. Mishchenko, L. Britnell, R. Krupke, K.S. Novoselov and C. Casiraghi, Probing the nature of defects in graphene by raman spectroscopy, *Nano letters,* **2012**, *12*(8), 3925.

128. S. Stankovich, D.A. Dikin, R.D. Piner, K.A. Kohlhaas, A. Kleinhammes, Y. Jia, Y. Wu, S.T. Nguyen and R.S. Ruoff, Synthesis of graphene-based nanosheets via chemical reduction of exfoliated graphite oxide, *Carbon,* **2007**, *45*(7), 1558-1565.

129. M. Kolb, R. Botet and R. Jullien, Scaling of kinetically growing clusters, *Phys. Rev. Lett.,* **1983**, *51*(13), 1123-1126.

130. F. Perrozzi, S. Prezioso and L. Ottaviano, Graphene oxide: From fundamentals to applications, *J. Phys.: Condens. Matter,* **2015**, *27*(1), 013002.

131. S. Koga, I. Katayama, S. Abe, H. Fukidome, M. Suemitsu, M. Kitajima and J. Takeda, High-frequency coherent phonons in graphene on silicon, *Appl. Phys. Express,* **2011**, *4*(4), 045101.

132. K. Ishioka, M. Hase, M. Kitajima, L. Wirtz, A. Rubio and H. Petek, Ultrafast electron-phonon decoupling in graphite, *Phys. Rev. B,* **2008**, *77*(12), 121402.

133. I. Calizo, A.A. Balandin, W. Bao, F. Miao and C.N. Lau, Temperature dependence of the raman spectra of graphene and graphene multilayers, *Nano letters,* **2007**, *7*(9), 2645-2649.

134. P. Zhao, A. Kumamoto, S. Kim, X. Chen, B. Hou, S. Chiashi, E. Einarsson, Y. Ikuhara and S. Maruyama, Self-limiting chemical vapor deposition growth of monolayer graphene from ethanol, *The Journal of Physical Chemistry C,* **2013**, *117*(20), 10755-10763.

135. L. Viikari, J. Vehmaanperä and A. Koivula, Lignocellulosic ethanol: From science to industry, *Biomass and Bioenergy,* **2012**, *46*, 13-24.

136. Chii-Chang Chen, H. Forte, A. Carenco, J.-. Goedgebuer and V. Armbruster, Phrase correction by laser ablation of a polarization independent LiNbO3 mach-zehnder modulator, *LPT,* **1997**, *9*(10), 1361-1363.

137. B. Wu and A. Kumar, Extreme ultraviolet lithography: A review, Journal of Vacuum Science & Technology B: Microelectronics and Nanometer Structures, 25, 2007, 1743-1761.

138. S. Borini, R. White, D. Wei, M. Astley, S. Haque, E. Spigone, N. Harris, J. Kivioja and T. Ryhänen, Ultrafast graphene oxide humidity sensors, *ACS Nano,* **2013**, *7*(12), 11166-11173.

139. S. Mao, G. Lu and J. Chen, Nanocarbon-based gas sensors: Progress and challenges, *Journal of Materials Chemistry A,* **2014**, *2*(16), 5573.